NAVAL POSTGRADUATE SCHOOL

MONTEREY, CALIFORNIA

THESIS

MEMS-BASED CAPACITIVE
GAMMA RADIATION DETECTOR

by

Nikolaos Vidalis

December 2023

Thesis Advisor: Dragoslav Grbovic
Co-Advisor: Craig F. Smith

Approved for public release. Distribution is unlimited.

THIS PAGE INTENTIONALLY LEFT BLANK

REPORT DOCUMENTATION PAGE			*Form Approved OMB No. 0704-0188*
Public reporting burden for this collection of information is estimated to average 1 hour per response, including the time for reviewing instruction, searching existing data sources, gathering and maintaining the data needed, and completing and reviewing the collection of information. Send comments regarding this burden estimate or any other aspect of this collection of information, including suggestions for reducing this burden, to Washington headquarters Services, Directorate for Information Operations and Reports, 1215 Jefferson Davis Highway, Suite 1204, Arlington, VA 22202-4302, and to the Office of Management and Budget, Paperwork Reduction Project (0704-0188) Washington, DC, 20503.			
1. AGENCY USE ONLY ***(Leave blank)***	**2. REPORT DATE** December 2023	**3. REPORT TYPE AND DATES COVERED** Master's thesis	
4. TITLE AND SUBTITLE MEMS-BASED CAPACITIVE GAMMA RADIATION DETECTOR			**5. FUNDING NUMBERS**
6. AUTHOR(S) Nikolaos Vidalis			
7. PERFORMING ORGANIZATION NAME(S) AND ADDRESS(ES) Naval Postgraduate School Monterey, CA 93943-5000			**8. PERFORMING ORGANIZATION REPORT NUMBER**
9. SPONSORING / MONITORING AGENCY NAME(S) AND ADDRESS(ES) N/A			**10. SPONSORING / MONITORING AGENCY REPORT NUMBER**
11. SUPPLEMENTARY NOTES The views expressed in this thesis are those of the author and do not reflect the official policy or position of the Department of Defense or the U.S. Government.			
12a. DISTRIBUTION / AVAILABILITY STATEMENT Approved for public release. Distribution is unlimited.			**12b. DISTRIBUTION CODE** A

13. ABSTRACT (maximum 200 words)

Personal radiation detectors can be used to detect radioactive sources, measure the dose of radiation exposure, or alert those exposed to radiation energy. Applications vary from law enforcement to medical, scientific, power generation and hazardous material (HAZMAT) detection. Most of the currently used dosimeters are either single-use film badges which do not provide a direct reading and need further treatment after irradiation exposure, or direct-reading electronic pagers which might have limited capabilities to measure accumulated dose. In this thesis the development of a micro-electromechanical systems (MEMS)-based gamma radiation detector was investigated. Research on a new approach that would bring compact, low-cost, low-power radiation sensing capabilities was conducted. Multiple detection configurations and materials were researched. For the purpose of the thesis, materials whose physical properties change upon interaction with gamma radiation energy sources were evaluated. Applicable methods to recover exposed material to its initial properties were investigated, so that repeatability of the measurements could be achieved. Manufacturing of miniaturized sensors by incorporating MEMS technology was eventually demonstrated. The possibility to develop a device about the size of a postage stamp to be plugged into a mobile device to detect and process sensor data was successfully investigated.

14. SUBJECT TERMS radiation detection, gamma, micro-electromechanical systems, MEMS			**15. NUMBER OF PAGES** 99
			16. PRICE CODE
17. SECURITY CLASSIFICATION OF REPORT Unclassified	**18. SECURITY CLASSIFICATION OF THIS PAGE** Unclassified	**19. SECURITY CLASSIFICATION OF ABSTRACT** Unclassified	**20. LIMITATION OF ABSTRACT** UU

NSN 7540-01-280-5500 Standard Form 298 (Rev. 2-89) Prescribed by ANSI Std. 239-18

THIS PAGE INTENTIONALLY LEFT BLANK

Approved for public release. Distribution is unlimited.

MEMS-BASED CAPACITIVE GAMMA RADIATION DETECTOR

Nikolaos Vidalis
Captain, Hellenic Air Force
BAE, Hellenic Air Force Academy (HAFA), 2010
MS, National Technical University of Athens (NTUA), 2017

Submitted in partial fulfillment of the
requirements for the degree of

MASTER OF SCIENCE IN APPLIED PHYSICS

from the

NAVAL POSTGRADUATE SCHOOL
December 2023

Approved by: Dragoslav Grbovic
Advisor

Craig F. Smith
Co-Advisor

Frank A. Narducci
Chair, Department of Physics

THIS PAGE INTENTIONALLY LEFT BLANK

ABSTRACT

Personal radiation detectors can be used to detect radioactive sources, measure the dose of radiation exposure, or alert those exposed to radiation energy. Applications vary from law enforcement to medical, scientific, power generation and hazardous material (HAZMAT) detection. Most of the currently used dosimeters are either single-use film badges which do not provide a direct reading and need further treatment after irradiation exposure, or direct-reading electronic pagers which might have limited capabilities to measure accumulated dose. In this thesis the development of a micro-electromechanical systems (MEMS)-based gamma radiation detector was investigated. Research on a new approach that would bring compact, low-cost, low-power radiation sensing capabilities was conducted. Multiple detection configurations and materials were researched. For the purpose of the thesis, materials whose physical properties change upon interaction with gamma radiation energy sources were evaluated. Applicable methods to recover exposed material to its initial properties were investigated, so that repeatability of the measurements could be achieved. Manufacturing of miniaturized sensors by incorporating MEMS technology was eventually demonstrated. The possibility to develop a device about the size of a postage stamp to be plugged into a mobile device to detect and process sensor data was successfully investigated.

THIS PAGE INTENTIONALLY LEFT BLANK

TABLE OF CONTENTS

I. INTRODUCTION 1
A. THESIS STRUCTURE AND EXPERIMENT OUTLINE 2
B. LITERATURE REVIEW 3
C. THESIS OBJECTIVE 5

II. BACKGROUND 7
A. RADIATION MEASURING DEVICES 7
1. Radiation Detectors 7
2. Radiation Dosimeters 8
B. RADIATION EFFECTS ON POLYMERS 9
1. Chain Scission 9
2. Crosslinking 10

III. SENSOR FABRICATION METHODS 11
1. MEMS Sensor 60x20 11
2. MEMS Sensor 60x30 11
3. MEMS Sensor 30x20 12
A. SENSOR CHIP FABRICATION 12
B. DIELECTRIC PASTE FABRICATION 19
1. Pure PVDF Dielectric Paste Capacitors 20
2. PVDF-Carbon Black Dielectric Paste Capacitors 21
C. RADIATION MEASURING PLATFORM 25
D. ISSUES AFFECTING EXPERIMENTAL CAPACITANCE MEASUREMENTS 26
1. Capacitance Measurements 27
2. Electrical Grid Power 27
3. Power Bank Sources 27
4. Laptop Connections 28
5. Electromagnetic Interference 28
6. Dicing 28
E. IONIZING RADIATION SOURCE 29
1. Absorbed Dose 32
F. SENSOR CAPACITANCE 36
1. Analytical Calculation of the Sensor Capacitance 37
2. Numerical Calculation of the Sensor Capacitance 40
3. Measuring the Sensor Capacitance 42

4. Results Comparison 43

IV. EXPERIMENTAL RESULTS 47

A. PURE PVDF MEMS SENSOR 47

1. Sensor Irradiation 47

2. Sensor Annealing 54

B. C-PVDF MEMS SENSOR 58

C. PVDF VERSUS C-PVDF MEMS SENSOR 64

V. CONCLUSIONS AND FUTURE WORK 67

A. CONCLUSIONS 67

B. FUTURE WORK 68

APPENDIX A. ARDUINO SCRIPT 69

APPENDIX B. MATLAB SCRIPT 73

LIST OF REFERENCES 77

INITIAL DISTRIBUTION LIST 81

LIST OF FIGURES

Figure 1. Radiation detectors and dosimeters. Source: [16]–[18] 9

Figure 2. SOI wafer 13

Figure 3. Photoresist application by spin coating.. 15

Figure 4. Pattern transfer process 15

Figure 5. Plasma etching and dimensional check of the MEMS chips 16

Figure 6. MEMS sensor dimensional check.. 17

Figure 7. Progression of fabrication of a MEMS capacitor 18

Figure 8. Radiation stability of selected medical grade polymers. Source: [21]...... 19

Figure 9. MEMS chip in a 16-pad chip reader 21

Figure 10. PVDF-carbon black dielectric paste application...................................... 23

Figure 11. MEMS sensors capacitance measurements 24

Figure 12. Baking cycles 25

Figure 13. Measuring configuration. a) Measuring platform, b) Cs-137 disk on clamshell chip testing box.. 26

Figure 14. Dicing problems... 29

Figure 15. Bohr model of cesium. Source: [24] 30

Figure 16. Cs-137 gamma radiation disk 30

Figure 17. Transmission factors. Source: [25] 31

Figure 18. Mass attenuation coefficient calculation set-up. Source: [7] 35

Figure 19. Gamma rays from source to sensor.. 36

Figure 20. MEMS sensor capacitive configuration... 38

Figure 21. 60x20 MEMS sensor simulation by using COMSOL. 41

Figure 22. MEMS capacitors and their recorded capacitance values......................... 43

Figure 23. PVDF sensor raw capacitance data 48
Figure 24. Noise in measurements 49
Figure 25. PVDF sensor outliners filtering 50
Figure 26. PVDF sensor total capacitance versus absorbed dose 51
Figure 27. PVDF sensor finger capacitance vs. absorbed dose 52
Figure 28. PVDF sensor finger capacitance changes 53
Figure 29. 60x20 MEMS sensor capacitance after annealing 54
Figure 30. Outliner filtering after sensor annealing 55
Figure 31. Annealed sensor capacitance 55
Figure 32. Annealed PVDF sensor irradiation 56
Figure 33. Capacitance measurements for the annealed sensor 56
Figure 34. PVDF sensor capacitance – 7-day re-exposure after annealing 57
Figure 35. White noise. Source: [31] 58
Figure 36. C-PVDF sensor raw capacitance data 59
Figure 37. C-PVDF sensor outliners filtering 60
Figure 38. C-PVDF sensor total capacitance 61
Figure 39. C-PVDF sensor finger capacitance 62
Figure 40. C-PVDF sensor finger capacitance changes 63
Figure 41. C-PVDF versus PVDF sensor comparison 64

LIST OF TABLES

Table 1. 100 mm diameter SOI wafer characteristics 13

Table 2. Aluminum film deposition recipe 14

Table 3. Cs-137 disk characteristics 32

Table 4. Capacitance values for an “empty” 60x20 MEMS sensor 44

Table 5. PVDF and C-PVDF results summary 65

THIS PAGE INTENTIONALLY LEFT BLANK

LIST OF ACRONYMS AND ABBREVIATIONS

Al	Aluminum
CNT	Carbon Nanotube
Cs-137	Cesium 137
DHS	Department of Homeland Security
EPD	Electronic Personal Dosimeters
ER-PRD	Extended Range Personal Radiation Detector
HAZMAT	Hazardous Materials Management
LED	Light Emitting Diode
MEMS	Micro-Electromechanical Systems
NDI	Non-Destructive Inspection
NDT	Non-Destructive Testing
OSHA	Occupational Safety and Health Administration
PERD	Personal Emergency Radiation Detector and monitor
PRD	Personal Radiation Detector
PVDF	Polyvinylidene Difluoride
RIID	Radioisotope identification Device
SEM	Scanning Electron Microscope
Si	Silicon
SiO_2	Silicon Dioxide
SOI	Silicon on Insulator
SPRD	Spectroscopic Personal Radiation Detector
SWCNT	Single Walled Carbon Nanotube

THIS PAGE INTENTIONALLY LEFT BLANK

ACKNOWLEDGMENTS

First and foremost, I would like to thank my advisor, Dr. Dragoslav Grbovic, for always coming up with out-of-the-box solutions every time insuperable problems would arise. His great experience in micro-electromechanical systems allowed for deep understanding of the nature of various MEMS issues. Building multiple sensors from scratch and testing them on real life applications has been a uniquely rewarding experience.

I would also like to thank Dr. Craig Smith for his advice and his guidance on the interpretation of the results that were derived from the radiation measurements. His great experience in radiation detection technology allowed for the presentation of the data in a way that is readily useful to the nuclear community.

I would especially like to thank William Melos Guimaraes and Thomas Stapel for their great support in the fabrication process of the MEMs chips. Their great experience allowed for multiple chip fabrication on a single wafer that would later offer increased testing capabilities.

Finally, I would like to thank Robo-Dojo, for the great support throughout my research. The provided training sessions on high-end technologies were of great help to multiple parts of this research. Robo-Dojo-provided hardware, such as the Arduino boards that were used for building the radiation dose measuring platform, allowed for experimenting with different equipment and finally matching experiment requirements to measuring methods.

THIS PAGE INTENTIONALLY LEFT BLANK

I. INTRODUCTION

Human beings and their man-made systems are exposed to ionizing radiation daily and, with added occupational exposure, may experience adverse effects. Multiple factors dictate the effects of exposure, including, but not limited to, the type of radiation source, its intensity, and the period of exposure. Radiation sources vary from artificially created sources to natural background radiation sources. Artificial sources may include medical equipment, such as sterilization devices and nuclear medicine procedures, nuclear weapons, nuclear power fuel, non-destructive inspection (NDI) equipment and numerous other man-made sources. Natural sources may include solar activity radiation, cosmic rays, terrestrial radiation and other naturally occurring radionuclides. Evidently, satellites and space systems in general undergo a continuous radiation exposure and their performance is greatly affected by solar activity [1]. High doses of radiation are absorbed by their sensor materials, leading to decreased performance or even permanent damage. Much current research investigates not only space sensor radiation shielding but also resetting and/or recovering already damaged sensors [1]. It is obvious that damaged sensor recovery capabilities in space will lead to increased performance, significant cost reduction and increased system reliability. NASA has also shown great interest in developing innovative techniques for «annealing» damaged sensors [2]. It is evident that minimizing ionizing radiation exposure effects is critical not only to human health but also to man-made system performance.

Real-time dosimetry capabilities would allow for better protection and handling of ionizing radiation sources and increased system performance. Active radiation shielding, multiple simultaneous measurements capabilities, and real-time sensor annealing/resetting, before decreased performance is observed, would increase space systems effectiveness and reliability. The Occupational Safety and Health Administration (OSHA) requires all employees with high risk of radiation exposure to wear radiation dosimeter badges. It is common that those dosimeters do not offer direct dose readings. Therefore, the wearable badges are sent for analysis and radiation absorbed dose calculation regularly. Real-time direct reading portable dosimeters are also used in some applications, but there is a need

for such devices that are small, inexpensive, and more versatile. Moreover, environmental concerns and rising needs for cleaner energy will eventually lead to greater nuclear power exploitation, increasing the needs for such improved real-time portable dosimeters. Consequently, by considering the wide spectrum of exposure to ionizing radiation sources, real-time dosimetry is of crucial importance to human health, safety, and system performance.

The increased needs for radiation dosimetry call for innovative sensing technology solutions. Those can come in the form of detection systems, capable of real-time, simultaneous real-time measurements performed on sensory data collected by miniaturized sensors. Wearables, smart phones, and other advanced devices are equipped with reliable high-performance micro-sensors. Based on the same philosophy, a miniaturized radiation sensor combining multiple techniques for measuring exposure to different types of radiation sources is suggested. MEMS technology along with the appropriate selection of sensing materials can be used for the fabrication of a radiation "nose" detector able to detect multiple ionizing radiation sources.

The great hands-on experience that currently exists at the Naval Postgraduate School (NPS) along with the great capabilities of the NPS Microsystems Fabrication Laboratory indicate a very promising future for building innovative sensors that outperform the existing industrial sensors.

A. THESIS STRUCTURE AND EXPERIMENT OUTLINE

The five chapters of this thesis outline the research, fabrication and finally the deployment of an innovative gamma radiation micro-electromechanical system (MEMS) sensor. Chapter I provides a general framework of the current research and communicates the importance of real-time radiation dosimetry. Chapter II provides the theoretical background, principles, and physics applicable to this research. Chapter III discusses the MEMS sensor fabrication process and the experimental procedure. Chapter IV provides the analysis of the results obtained by the deployment of the MEMS sensors. Chapter V provides the conclusion of the research and suggests ideas for future work.

B. LITERATURE REVIEW

Much research has been performed in the fields of ionizing radiation dosimetry during the last decade [1], [3], [4] since the need for control and measurement of exposure to radiation-emitting sources is crucial not only for human health but also for ensuring system performance and reliability. Different types of radiation sensors have been researched in an effort to satisfy the growing needs of space [1] , nuclear [5], [6], medical [7], remote sensing [8], non–destructive testing (NDT) [9] and other industrial applications. Gamma radiation sensors capable of offering direct and reliable readings of exposure in a cost-effective way have been greatly investigated.

Throughout multiple studies, a wide range of materials whose properties change when exposed to gamma radiation sources have been tested. When it comes to radiation exposure effects, it is the electrical and mechanical properties of the selected materials that are the primary area of concern. Significant changes in resistance [8], capacitance [9] and elongation [10] with exposure have been observed in many studies. Materials under research, range from metal oxides [11], [12] to polymers [13]. Changes on the electrical properties due to the depolymerization of organic-based materials, when exposed to ionizing radiation, seem to indicate a promising solution to the use of MEMS technology for real-time radiation detection and dosimetry [14]. A decreasing resistance and an increasing capacitance have been evidenced with the increase of the radiation dose absorbed by polyvinylidene fluoride (PVDF) films. Similar results have been obtained in both PVDF-carbon black composite thick films [9] and in carbon nanotubes composites [14] when exposed to gamma radiation sources. Polymer pastes enriched with carbon black composites for increased conductivity showed a monotonic tenfold increase in the values of the current as a result of the decreased resistance. On the same basis, observations of significant capacitance increase have been witnessed for less conductive composites, with a low percentage of carbon doping [9].

Ribeiro et al. [13] have showed that pure PVDF films irradiated with 15 kGy [1] experience changes in their mechanical properties. The PVDF films, used in their research, underwent both a tensile strength and an elongation at rupture decrease with radiation dose. The same study showed that low radiation doses do not seem to affect the mechanical properties of the polymers in a significant way. It is evident that most polymers have a satisfactory radiation tolerance to doses lower than 100 Gy [3].

On the other hand, the prolonged exposure to cosmic radiation affects the space systems and especially their electronic component performance [15]. Electric circuits incorporate multiple capacitors and MOSFET transistors whose performance depends on the inherent properties of the dielectric material. Common materials used as dielectrics are mainly insulators whose properties might be changed after prolonged exposure to ionizing radiation. High doses of radiation absorbed allow a significant number of electrons to leave the valence band and move to the conduction band. Free carriers and electric dipole changes might affect the dielectric permeability and render a system unreliable. More research on ceramic capacitors [1], used in space applications, showed a significant change in the measured capacitance with exposure to cosmic rays. Therefore, improved shielding or compensation circuitry can be deemed necessary for ensuring system reliability. Additionally, the temporary gamma radiation effects on the ceramic capacitors were perceived as a potential application for gamma radiation detection and/or ionizing radiation dosimetry, following a nuclear accident event.

Finally, similar effects on the properties of oxide thin and thick films were observed upon exposure to gamma radiation [11]. The oxide-based radiation sensing layers underwent significant electrical and optical property changes with the increase in radiation dose. Both the thin and the thick films showed current-voltage characteristics dependencies on the radiation absorbed doses.

---

[1] The Gray (Gy) is a unit used to measure the amount of radiation absorbed dose. In the international system of units (SI), one Gray (Gy) is equal to an absorbed dose of 1 Joule/kilogram and reflects the amount of ionizing radiation energy deposited in materials.

C. THESIS OBJECTIVE

Within the aforementioned framework, the main objective of this thesis is to develop a novel gamma radiation sensor for real-time dosimetry measurements. A fabrication process by means of MEMS technology will allow for sensor miniaturization. The sensor design requirements are summarized as follows:

1. Inexpensive: Readily available materials and mass production capabilities have been considered for low-cost sensor manufacturing
2. Miniaturized: Small scale sensors able to be incorporated in portable electronic devices such as wearables and smart phones.
3. Low-powered: Low power demand will allow for prolonged use.
4. Re-usable: Resetting/Annealing dosimetry sensor will allow for reusability and extended sensor operation lifetime.
5. Real-time direct reading capability: Dosimetry measurements in real-time will allow for increased health and safety protection or reliable and effective system operation.

Some areas of concern that had to be addressed before the final sensor design stage:

1. What common inexpensive materials could be used for building the sensor?
2. How would a miniaturized sensor respond to radiation exposure when compared to the bigger sized sensors of the existing studies made of the same materials?
3. How could we reset/anneal a sensor to the initial zero absorbed dose value?
4. Which inherent qualities of the materials selected could work towards getting real-time sensory readings?

THIS PAGE INTENTIONALLY LEFT BLANK

II. BACKGROUND

A. RADIATION MEASURING DEVICES

Exposure to radioactive sources can be detected by various ionizing radiation measuring devices. Radiation detectors and radiation dosimeters are used to measure the levels of radiation produced by a source and the amount of energy deposited by radiation in matter, respectively. Both detectors and dosimeters are capable of detecting ionizing radiation of some level; however, their operating principles may differ significantly. Dosimeters are a type of radiation detector used specifically for measuring the amount of energy deposited by radiation in matter. The most commonly used types of radiation detectors, based on the operating principles, include:

- Solid-state radiation detectors
- Gas-filled radiation detectors
- Scintillation detectors

1. Radiation Detectors

Radiation detectors are sensors used to detect exposure to radioactive sources. They are highly accurate and reliable devices, with some even featuring real-time displays of multiple radiation related parameters or offering exposure alert capabilities. Personal Radiation Detectors (PRDs), are smaller-sized detectors that are portable and allow the wearer to have instant awareness of the prevailing radiation levels. While detectors may offer enhanced radionuclide identification capabilities by measuring the energy spectrum of the emitted radiation, they may not provide information on the accumulated absorbed radiation dose, which can be crucial both for human health and for system performance.

Some common types of portable radiation detectors include:

- Personal Emergency Radiation Detectors and monitors (PERDs)
- Non-alarming PERDs

- Personal Radiation Detectors (PRDs)
- Spectroscopic PRDS (SPRDS)
- Extended Range Personal Radiation Detectors (ER-PRDs)
- Radioisotope identification Device (RIID)

2. Radiation Dosimeters

Radiation dosimeters are used to measure the absorbed dose of the ionizing radiation by recording the system's accumulated exposure. Active sensing dosimeters can detect real-time radiation exposure and may even come with a display. However, they are often significantly larger and more expensive due to their power requirements or complexity. Passive sensing dosimeters, on the other hand, are considerably smaller and lighter in weight, as they do not require power to operate. However, passive dosimeters need to be removed and further processed for the stored signal to be read out, as they operate in the cumulative mode. Although there are passive dosimeters that allow readings using other portable equipment, this is still an asynchronous measuring technique as the reading is performed either before or immediately after the exposure.

Common types of dosimeters, as shown in Figure 1, include:

- Handheld survey meters
- Personal dosimeters
- Portable ionization chambers
- Electronic personal dosimeters (EPD)

Figure 1. Radiation detectors and dosimeters. Source: [16]–[18]

B. RADIATION EFFECTS ON POLYMERS

Polymers exposed to radioactive sources for extended periods of time tend to show changes in their inherent properties due to chemical ageing effects known as chain scission and crosslinking. Although those two phenomena take place simultaneously within the material structure, their effects and magnitude differ according to the material composition. Most of the time there, only one dominant process will define the changes of the material properties. In general, the tensile strength of the materials is directly proportional to the crosslinking magnitude and inversely proportional to the chain scission effects, while the material elongation is only proportionally related to both mechanisms. Chain scission and crosslinking tend to increase material elongation [10]. As these changes are closely related to the material composition, careful selection of materials and their additives can be made to control the intensity of the radiation exposure effects. Therefore, appropriate material selection must be made after a thorough investigation of the chain scission and crosslinking phenomena. Polymer degradation assessment should also include a thorough investigation of the crosslinking and chain scission effects by using direct or indirect methods. Infrared and Raman spectroscopy, chemiluminescence, nuclear magnetic resonance and mechanical properties testing are just some of the methods that may be used to evaluate chemical ageing effects.

1. Chain Scission

Polymers are composed of macromolecules linked over polymer chains. Chain scission could act as a degradation / depolymerization mechanism that ruptures the bonds

of those polymer chains reducing polymer's molecular weight. This can occur due to thermal stress, exposure to ionizing radiation or a combination of both. The depolymerization of the polymer leads to degradation of the elastic properties and lower cross-link density within the material. This results in a decrease in material strength and an increase in material elongation.

2. Crosslinking

Crosslinking is another form of polymer degradation that results in new polymer chain linkages. Cross-links can be formed due to various factors, including pressure, heat, and irradiation. The new longer chains increase the overall structure rigidity, leading to changes in the mechanical properties of the polymer change. By creating stable and rigid polymer structures, molecule slipping is prevented, and crosslinking may, among others, improve the impact resistance, increase the tensile strength, offer better electrical resistance and enhanced dielectric properties. The extend of changes is greater as the crosslink density increases. Intentional and controlled crosslinking can be achieved by adjusting the parameters of radiation exposure along with the material composition.

It is expected that both chain scission and crosslinking will affect the configuration and the mobility of the dipoles within the material and therefore impact the way the material interacts with the electric field. This is then manifested in the dielectric properties and relative dielectric constant in particular. Monitoring the capacitance is the best way to evaluate and monitor the change in dielectric constant.

III. SENSOR FABRICATION METHODS

The current research aims to fabricate a small-sized sensor using MEMS technology, with the sensor's principal structural element being an interdigitated finger capacitor configuration designed and manufactured at the NPS Cleanroom. This design is a common MEMS configuration used for sensing accelerations, sound etc.[19] and offers increased capacitance for a given cross-section, enabling the fabrication of small-sized sensors. The COMSOL Multiphysics 6.0 software system has extensively been used for the design and simulation needs of the MEMS chips. The chip capacitance values obtained by simulation were compared to the experimentally collected measurements. Additionally, the MEMS PRO software was used as the primary software for simulating the fabricating procedure.

For detecting and measuring the absorbed dose of gamma radiation during exposure, the sensing element of the radiation detector is a MEMS chip with a PVDF and PVDF-carbon black enriched paste applied as the dielectric material of the chip capacitor. To improve cost-effectiveness, speed and repeatability, multiple chips with similar shapes but different geometric properties were fabricated on a single silicon wafer.

1. MEMS Sensor 60x20

This has been the principal sensing configuration used throughout the entire experimental process for the pure PVDF sensors. A MEMS capacitive sensor having sixty (60) fingers (30 on each electrode) and a 20μm spacing between them was proved to be an efficient sensing configuration offering high capacitance readings. The results presented in this thesis for the 60x20 configuration are related to sensors using pure PVDF rather than a PVDF- carbon black composite. The interpretation and final analysis of the collected information are all based on this sensing geometry and dielectric material.

2. MEMS Sensor 60x30

The use of MEMS capacitive sensors with sixty (60) fingers (30 on each electrode) and a 30μm spacing between them would allow for deeper penetration of the dielectric

paste which could eventually lead to greater sensitivity, at least theoretically. However, in practice the increased spacing between the fingers led to lower capacitance values. Therefore, the 60x20 geometry was preferred over the 60x30 sensor.

3. MEMS Sensor 30x20

MEMS capacitive sensors having sixty (60) fingers and a 20μm spacing between them would offer higher capacitance values when compared to the chips with fewer interdigitated fingers. However, applying the PVDF-carbon black dielectric paste to the 60-finger configuration would lead to short-circuiting and clogging issues, rendering the chips ineffective. Although the application of the dielectric paste over chips with different cross-sectional configurations would make any comparison among the sensors difficult, the 30x20 sensing configuration was eventually preferred for the C-PVDF chips due to its consistent and satisfactory results.

A. SENSOR CHIP FABRICATION

A Silicon on Insulator (SOI) wafer was chosen as the substrate on which to deposit the structural material. The SOI wafer contains a thin layer of silicon dioxide acting as an insulator between the silicon substrate and the top silicon layer, as depicted in Figure 2. SOI wafers are widely used in the semiconductor industry due to their high performance and their high performance and low power consumption. They allow for the fabrication of multiple chips, reducing cost and increasing testing capabilities. The capacitor plates, in the form of interdigitated fingers, would be made of a silicon (Si) device layer with a thin layer of aluminum (Al) on top, used to serve as an improved electrical contact.

Figure 2. SOI wafer

The selected silicon (Si) – silicon dioxide (SiO_2) characteristics of the wafer are shown in Table 1.

Table 1. 100 mm diameter SOI wafer characteristics

Device Thickness	30+/-1um	Lot #	UD-13858 / UH-13857
Device Resistivity	.005-.025 ohm-cm	Type-Orient:	P/B (1-0-0)
Handle Thickness	275+/-25um	Box: ON D	3um +/-5%
Handle Resistivity	.005-.025 ohm-cm	Qty:	25 pcs

To deposit a homogeneous thin aluminum film on the entire SOI wafer, an additive deposition process was used (Figure 7b). During the aluminum deposition prosses, critical operating parameters of the Angstrom Nexdep sputter coater, such as the rate of material deposition and the thickness of the aluminum film, were continuously monitored to ensure a high-quality structural layer. Finally, a uniform 100nm thin film of aluminum was deposited on the top side of the SOI wafer. The aluminum deposition recipe parameters are detailed in Table 2.

Table 2. Aluminum film deposition recipe

Start up	Estimated Duration	25min
Substrate Rotation	Substrate Velocity	10RPM
Configure Pulse DC Supply – Ignite Plasma	Operation Mode	DC-Arc Detect
	Pulse Frequency	0
	Reverse Time	0
	Delay Time	60s
	MFC 3 Flow Rate	20 SCCM
Ramp Power – Ignite Plasma	Target Output	5%
	Ramp Rate	20 (%/min)
	Soak Time	30s
Process Pressure Dep Chamber	Pressure Setpoint	5mTorr
	Pressure Bump	Enabled
Ramp to Deposit Power	Target Output	20%
	Ramp Rate	30 (%/min)
	Soak Time	60s
Calibrate Rate	Delay Calibration Start Time	30s
	Sample Time	60s
Deposit Calibrated Rate	Thickness	1000A
Post Condition – Ramp Power	Target Output	0%
	Ramp Rate	20 (%/min)
	Soak Time	0s

A mask layer deposition followed the aluminum film application. A uniform layer of photoresist was first deposited and then patterned to allow for selective removal of the photoresist. The deposition process was performed in a UV-filtered lighting room. The photoresist application was performed while the wafer was spinning at 3000 rpm for 45 seconds to achieve maximum uniformity, as shown in Figure 3. A change in wafer color due to light scattering, was observed after the photoresist deposition process had been completed.

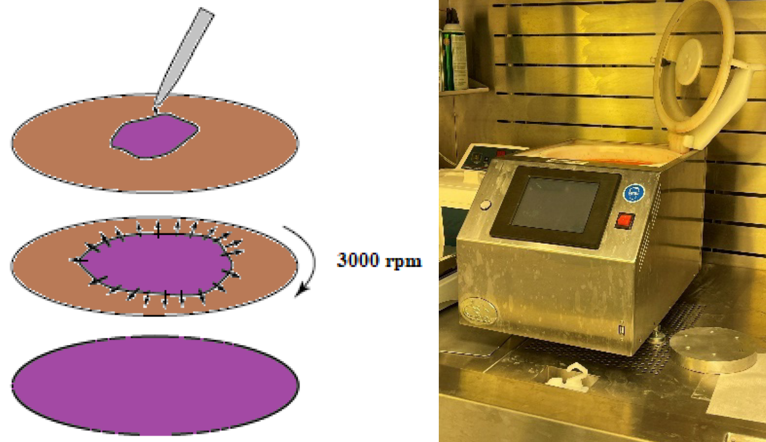

Figure 3. Photoresist application by spin coating

Photoresist hardening was achieved by means of soft baking at 90°C for 90 seconds. The wafer was then placed on a cooling plate for 30 seconds to allow for faster cooling.

Appropriate masking and patterning of the photoresist layer allowed for exposure of the surfaces that needed to be etched. The chip design pattern transfer was achieved through a common lithography patterning procedure, as shown in Figure 4.

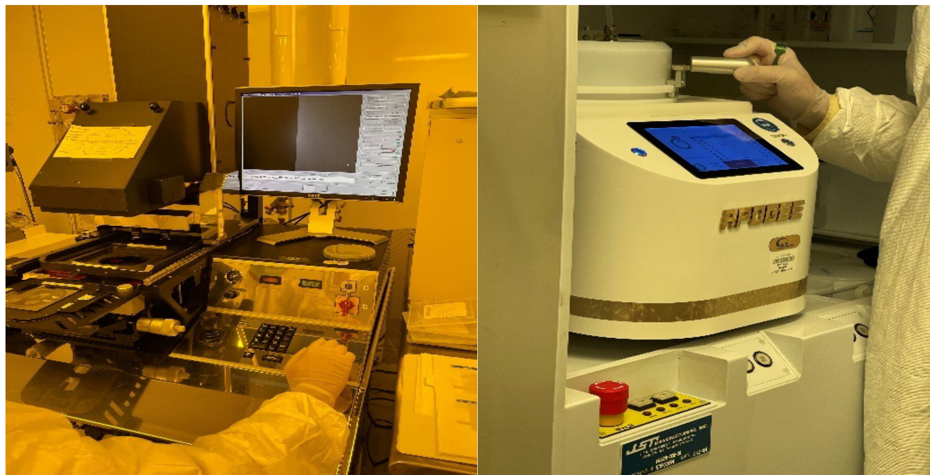

Figure 4. Pattern transfer process

After copying the pattern to the mask by exposing the photoresist layer to UV light in the EVG 620 contact aligner, development and removal of the photoresist were achieved

through an Appogee spin developer. A hard bake step was then performed at 12ºC for 90 seconds. The wafer was then placed on a cooling plate for 30 seconds to allow for faster cooling. During the photoresist development step, the photolithographic mask layer was removed over selected regions to expose the future channels between the aluminum interdigitated fingers. Aluminum wet etching with Sigma Aldrich Aluminum Etchant was used to remove the exposed aluminum (Figure 7c). This step was followed by Deep Reactive Ion Etching (DRIE) using the Bosch process [20] and the Oxford Instruments Plasmalab 180 ICP Etcher to etch the full depth of the SOI's device top silicon layer (30 μm). This created the channels between the interdigitated fingers of the MEMS capacitor.

Thirty (30) cycles of Bosch etching were performed before the capacitor channels were fully etched away. The wall thickness of the channels was carefully monitored to avoid thin wall collapse because of etching undercuts. Finally, the wafer was etched by using oxygen plasma in the Trion Sirus T2 Reactive Ion Etcher to allow the complete removal of the hardened photoresist (Figure 7d).

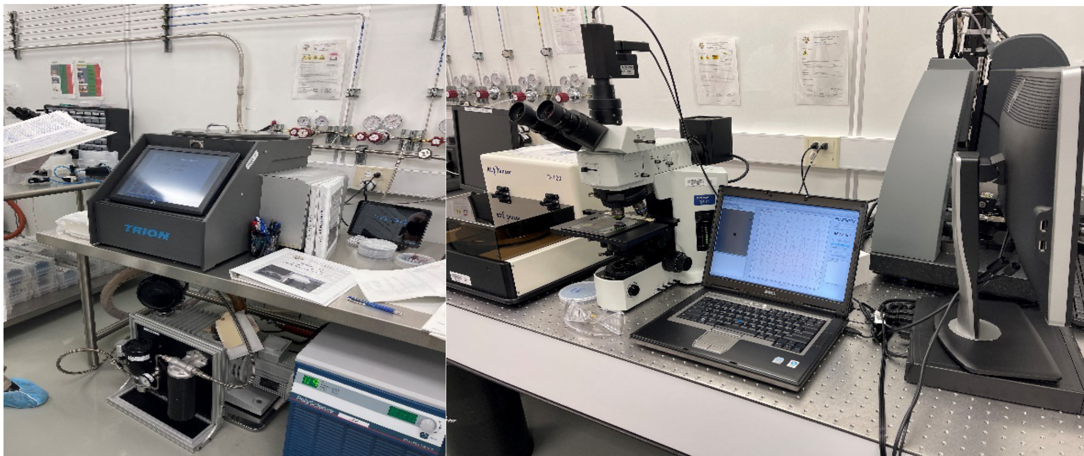

Figure 5. Plasma etching and dimensional check of the MEMS chips

Numerous quality checks were performed as the final steps of the fabrication procedure, as shown in Figure 6. Dimensional checks, unobscured and non-short-circuited

channels, sufficient channel etching and quality of the structural material were verified before proceeding to the next steps. Dicing[2] of the chips was performed as necessary.

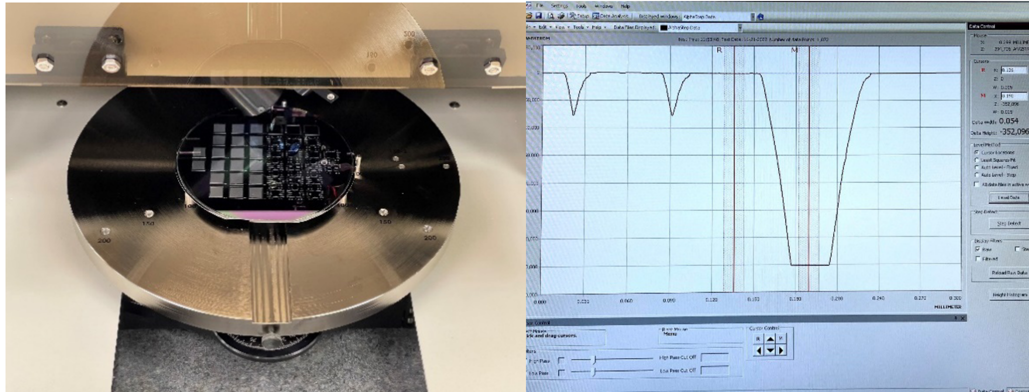

Figure 6. MEMS sensor dimensional check

[2] Dicing is the process by which the functional integrated circuits fabricated on a wafer are separated.

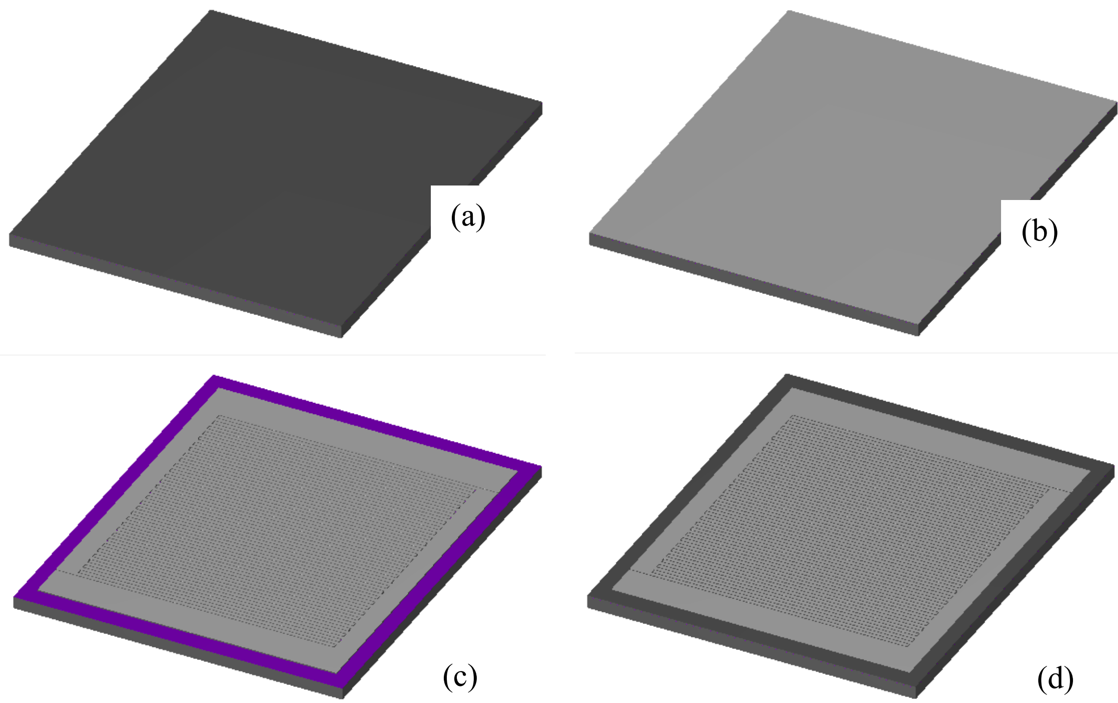

Figure 7. Progression of fabrication of a MEMS capacitor. Frame (a) is the top view of the wafer. Frame (b) is the aluminum layer deposition. Frame (c) patterning and selective removal of the photoresist. Frame (d) finished chip

B. DIELECTRIC PASTE FABRICATION

Although polymers in general show good tolerance to ionizing radiation, previous research has shown that extended ionizing radiation exposure may lead to changes in their structure due to depolymerization and/or changes in the polymer's visual properties. A wide range of polymers was considered for potential candidates for the fabrication of the dielectric paste of the MEMS capacitors. Some of the polymers considered for testing along with their radiation exposure characteristics can be seen in Figure 8.

MATERIAL	TOLERANCE LEVEL (KGY)	COMMENTS
Fluoropolymers		
Tetrafluroethylene (PTFE)	5	Liberates fluorine gas, disintegrates to powder. Avoid use.
Polychlorotrifluoroethylene (ECTFE)	200	
Polyvinyl Fluoride	1,000	
Polyvinylidene Fluoride (PVDF)	1,000	
Ethylene-Tetrafluoroethylene (ETFE)	1,000	
Fluorinated Ethylene Propylene (FEP)	50	Avoid use.
Polyacetals (Delrin, Celcon)	5	Avoid use due to embrittlement.
Polypropylene, Radiation Stabilized		
Homopolymer	20-50	Subject to orientation embrittlement. Validate with real time aging.
Copolymers of Propylene-Ethylene	25-60	More stable than Homopolymer.
Polypropylene, natural	20	Avoid use of unstabilized polypropylene.
Polystyrene	10,000	All styrenes are stabilized by Benzene ring structure.
Polysulfone	10,000	Amber colour before irradiation.
Polyurethane	10,000	Excellent clarity and chemical resistance to stress-cracking. Drying is essential.
Polyvinylbutyral	100	Yellows.
Polyvinylchloride (PVC)	100	Yellows, can be tinted for colour correction.
Polyvinylidene Chloride (PVDC)	100	Yellows, releases HCL.
Styrene/Acrylonitrile (SAN)	1,000	Yellows at 40 kGy.

Figure 8. Radiation stability of selected medical grade polymers. Source: [21]

After considering the tolerance limits of multiple polymers, it was their susceptibility levels to ionizing radiation that could be used as the main criterion for the selection of the dielectric paste material. However, polyvinylidene fluoride (PVDF) was finally selected for its high availability, low cost, easy manufacturing process, the great existing research, and its wide application in electronic devices.

1. Pure PVDF Dielectric Paste Capacitors

After considering the existing research on the effects of ionizing radiation on polymers, a pure PVDF paste was created and used as the dielectric material between the interdigitated fingers of the MEMS capacitor. Polyvinylidene fluoride (PVDF) is an inert thermoplastic fluoropolymer known for its resistance to solvents, acids, and hydrocarbons. It has a low density of 1.78g/cm^3 and a melting point of about 175ºC.

For the fabrication of the PVDF paste, PVDF powder purchased from Sigma-Aldrich was used. The PVDF powder was added to 7 wt.% ethyl cellulose (with a 48.0-49.5% w/w ethoxyl basis) and Terpinol-a, which acted as the primary solvent, to achieve a homogeneous and uniform mixture. Additional Terpinol-a was added, and the mixture was repeatedly mixed at 3000 rpm for one minute until satisfactory dispersion and homogeneity was achieved. The process of adding solvent and mixing was repeated until a uniform mixture was obtained. All mixing processes were performed in ambient room conditions.

After a homogeneous mixture was obtained, the PVDF paste was applied to the chip's interdigitated capacitors. The MEMS chip was left undisturbed for 24 hours to allow the paste to penetrate the grooves between the interdigitated fingers of the chip. Capacitance measurements were taken just before and immediately after the 24-hour waiting period, and no significant changes were observed. All chips were baked at 100ºC for 30 minutes followed by annealing at 170º C for 10 minutes. After the heat treatment was completed, new capacitance measurements showed a slight increase of about 10% in the total chip capacitance. The PVDF dielectric application had a positive effect on the MEMS chips capacitance.

Finally, the MEMS chips were plugged into the clamshell chip testing platform (Figure 9) and their capacitance was measured and monitored for a minimum period of

three days before they were exposed to ionizing radiation. Keeping the chips in the measuring platform until the capacitance stabilized proved to be an important part of the experimental process to avoid fictitious observations.

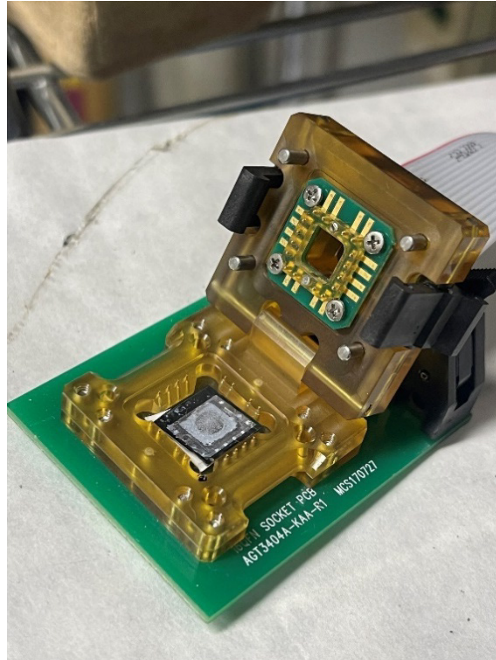

Figure 9. MEMS chip in a 16-pad chip reader

2. PVDF-Carbon Black Dielectric Paste Capacitors

In addition to the pure PVDF dielectric paste, a PVDF-carbon black enriched (C-PVDF) dielectric mixture was created. Previous work on similar mixtures has shown that the addition of carbon black particles can result in a higher capacitance by creating long carbon chains that allow for increased electron tunneling [22]. Furthermore, the addition of carbon black or carbon nanotubes can have a greater effect on the depolymerization of the polymer dielectric paste when exposed to ionizing radiation. However, previous work, , was based on devices of greater dimensions compared to the MEMS chips fabricated at

the NPS. This allowed researchers to create and deploy carbon-rich dielectric pastes below the percolation limit [9] without short-circuiting issues that would render the capacitors ineffective. Carbon-enriched PVDF composites containing approximately 3–7% wt. carbon black have been effectively deployed in many previous studies [23].

In this study, however, PVDF-carbon black composites with a carbon black to PVDF ratio of 3% wt. or greater always short-circuited the interdigitated fingers of our MEMS capacitors. The risk of carbon particles shorting the capacitors increased as the gap between the interdigitated fingers decreased. The application of such mixtures over the chip channels resulted in a decreased resistance between the silicon chip pads, indicating that the interdigitated fingers had been clogged by carbon black particles. By continuously decreasing the amount of the carbon black particles, a satisfactory threshold of about 1% was achieved.

To produce the carbon-enriched PVDF dielectric paste a combination of additives was used as reported in the Korostynska et al. paper [9]. Carbon nanopowder with a particle size smaller than 500nm bought from Sigma Aldrich was added to decaethylene glycol mono-dodecyl ether, which acted as a nonionic surfactant. The surfactant was absorbed onto the surface of the carbon particles and acted as a barrier to minimize particle–particle interaction, prevent recombination of carbon black particles, and avoid the formation of long carbon chains (clumping). The percolation threshold had to be carefully considered to avoid phenomena that could render the capacitive chips inoperative by shorting the electrodes. Finally, Terpinol-a was added to the mixture as a solvent. The quantity of Terpinol-a had to be adjusted to the amount of the carbon black particles so that an even dispersion of the carbon particles could be achieved. Multiple mixing cycles at 3000 rpm for 1 minute were performed until a homogeneous mixture was finally obtained.

To fabricate the dielectric paste, PVDF powder bought from Sigma-Aldrich was added to the carbon composite. A combination of 7% wt. Ethyl Cellulose of 48.0-49.5% w/w ethoxyl basis along with Terpinol -a were added in quantities that allowed for a homogeneous and uniform mixture. Mixing at 3000 rpm for 1 minute was repeatedly performed until satisfactory dispersion and homogeneity was achieved. Solvent was continuously added and the mixing process at 3000 rpm was repeated, until a uniform

mixture was finally obtained. The mixing process was performed under ambient room conditions.

The PVDF-carbon black dielectric paste had to be left undisturbed in an airtight plastic container under ambient room conditions for a week before its application over the MEMS capacitor. Allowing the paste mixture to settle for an extended period of time would allow the heavier particles, and therefore the long carbon chains, to settle on the bottom of the container. After the PVDF-carbon enriched dielectric mixture had been left untouched for a week, its application over the capacitive MEMS chips followed. At the time of the dielectric paste application, the part of the mixture laying closer to the surface was preferred to eliminate the presence of large carbon chains that would short-circuit the capacitors. Therefore, the final applied mixture possibly had a carbon black particle percentage lower than the nominal 1% wt. The surface area of the capacitor was then partially covered with the dielectric paste to allow for the trapped air to escape during the liquid mixture penetration into the gaps between the interdigitated fingers. Multiple parameters such as room temperature, liquid mixture viscosity, and applied pressure, could influence the penetration depth of the dielectric paste into the narrow channels separating the interdigitated fingers of the MEMS capacitor. After the paste application over the interdigitated fingers, the MEMS chip was left untouched for three (3) days to allow for deeper penetration.

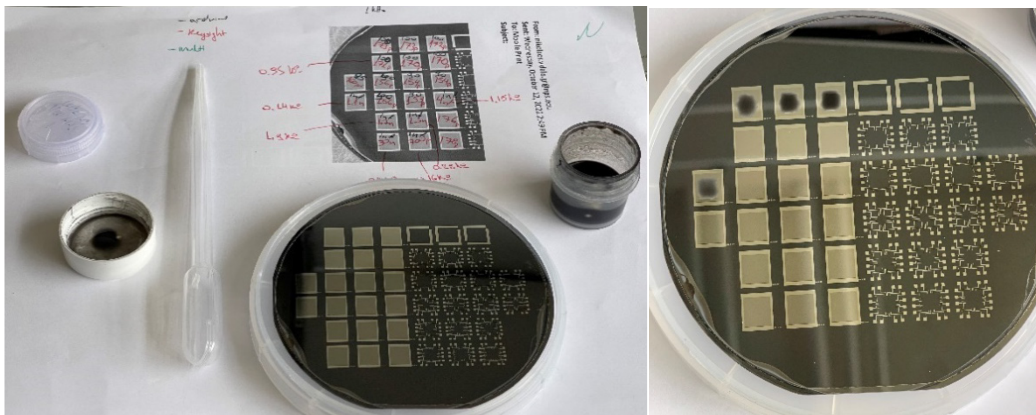

Figure 10. PVDF-carbon black dielectric paste application

During the fabrication process of the MEMS sensors, multiple measurements, as shown in Figure 11, had to be performed to record and monitor any significant capacitance changes. The capacitance values were collected using three (3) different measuring devices, an Arduino Board with a capacitance measuring script, a Keysight parameter analyzer device, and a standard multimeter. Similar capacitance values and trends were recorded by all measuring devices.

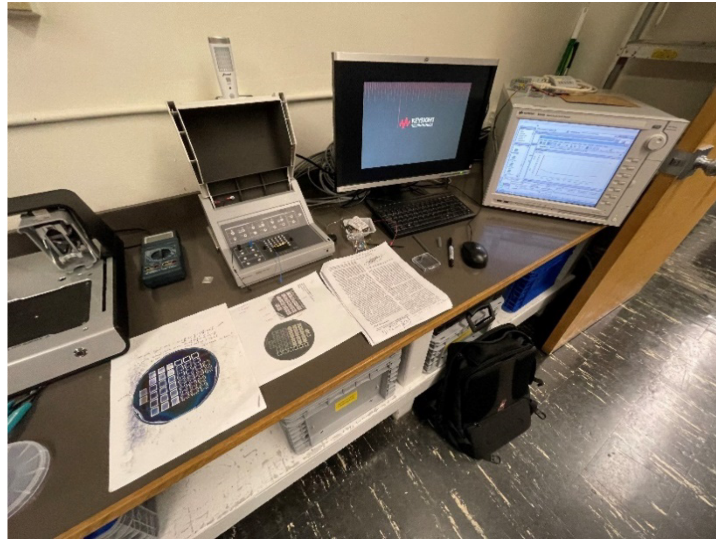

Figure 11. MEMS sensors capacitance measurements

After the 3-day settling period, the capacitance values of the chips were measured and compared to the "empty" MEMS capacitors. No significant changes were observed during the measurements following the liquid dielectric paste application. Baking at 100°C for 30 minutes followed by another baking cycle at 170°C for 10 minutes was finally performed over all MEMS chips, as shown in Figure 12. After the first baking cycle a capacitance increase of about 5–10% was observed. However, no significant changes in capacitance were observed after the second baking cycle.

Figure 12. Baking cycles

C. RADIATION MEASURING PLATFORM

For a deeper understanding of the gamma irradiation effects on the MEMS capacitive sensors, continuous, real-time measurements and capacitance recordings were deemed necessary. A 16-pad chip reader, an Arduino ELEGOO MEGA 2560 Board, and a laptop were used as integral parts of the measuring platform.

A 16-pad chip reader was the primary adapter through which the Arduino platform was connected to the MEMS sensors via a 5-inch cable, as shown in Figure 13. The Arduino ELEGOO MEGA 2560 Board was connected to a LED display for direct readings while the whole measuring platform was connected and powered by a laptop which was also used for real-time recordings and capacitance value monitoring. All measurements as recorded and displayed on the laptop screen were systematically compared to the LED indications for validation purposes. All values were recorded using the Tera Log software which at the time of the research, was available to download online.

Figure 13. Measuring configuration. a) Measuring platform, b) Cs-137 disk on clamshell chip testing box

All measurements were performed with the MEMS sensors placed in the 16-pad chip reader. The radiation disk was placed on top of the clamshell chip reader. A round thick steel enclosure was used to prevent ionizing radiation leakage and unintended exposure. Before irradiating the MEMS sensors with gamma rays, multiple measurements needed to be performed over an extended period of about one week to allow for establishing the capacitance baseline. Prevention of any fictitious fluctuations due to electromagnetic interferences was another issue that had to be seriously taken into consideration. Power supply instability (power bank, infrastructure electricity, laptop power etc.), steel enclosure interference and wiring effects had to be taken into consideration for reliable measurements to be obtained. Multiple adjustments were made to various parameters before finalizing the experimental configuration.

D. ISSUES AFFECTING EXPERIMENTAL CAPACITANCE MEASUREMENTS

Troubleshooting has been an important but time-consuming part of this research. Several issues that arose during the experimentation procedure have been successfully addressed.

In this section a brief description of the major problems that were addressed during the current research is given. The information stated here will allow for easier and unobscured future research, helping researchers address and eliminate fictitious

observations on time. The experimental process, being time consuming, does not allow for in situ corrections. Therefore, having a record of possible issues that might affect the experimental outcomes would help researchers be more efficient and consequently take the radiation detection research one step further.

1. Capacitance Measurements

It is critical for the researcher to understand how different power sources affect the outcome and consequently the analysis and the interpretation of the experimental results. For the scope of this research, multiple power sources were used to power the measuring platform assembly before the selection of the final power source was made. Connection to the infrastructure's power grid, power banks that provide DC current and standard Laptop USB 2.0 powered connections each had different effects on the collected capacitance measurements.

2. Electrical Grid Power

It was observed that powering the measuring platform assembly via common sockets would add excess noise to the capacitance measurements. Fluctuations in the electrical grid power could cause fictitious capacitance measurements that might be misinterpreted as changes in the sensor's capacitance values and attributed to the absorbed radiation. Capacitance measurements at the pico and nano scale are very sensitive to any power fluctuations and may even make it impossible to correctly interpret the results. In such cases, the use of a combination of Uninterruptible Power Supplies (UPS) and high-quality surge protectors is highly recommended.

3. Power Bank Sources

Powering the measuring platform assembly using power banks proved to be an efficient way to obtain reliable capacitance measurements. A power bank providing two (2) Amps to the measuring platform has been used effectively, and any noise in the observed measurements would be within acceptable limits for the experimentation procedure. However, extended periods of exposure to ionizing radiation sources would possibly require prolonged power supply. The use of a single power bank source might not

allow for full observation of the radiation exposure phenomena. Replacing power banks during the experimentation procedure should be strongly discouraged, as abrupt power changes might lead to irreversible capacitance-related phenomena.

4. Laptop Connections

A standard 2.0 USB laptop-to-platform connection was used both for powering the measuring platform and for data collection. This was by far the most efficient method to obtain reliable measurements and, therefore, it has been preferred over all other methods. Laptop settings should allow for uninterrupted and continuous operation. Running tasks and activities that might affect power supply, such as updates installation or device sleeping should be avoided.

5. Electromagnetic Interference

Extreme care must be given when it comes to electromagnetic interference effects that might induce currents to the wiring connections of the measuring platform. Appropriate shielding would help eliminate such phenomena. Exposed electrical circuits should by no means be in touch with the shielding structure as this might affect the capacitance observations. Any unintentional contact with metallic parts could lead to changes in the total circuit resistance and therefore unreliable capacitance measurements might be observed.

6. Dicing

Much care must be taken when dicing the MEMS chips fabricated on the SOI wafer. Apart from any obvious issues that might occur, such as wafer cracking or even complete chip destruction, dicing might also lead to malfunctioning or even non-operating chips, as shown in Figure 14. During the dicing process, particles detached from the wafer might land in the chip channels and eventually short-circuit the chip capacitor. Higher than expected capacitance values might be an early indication of channel clogging because of detached particles. The total circuit capacitance is calculated based on the "RC" time constant, and therefore any unintentional change in resistance would result in incorrect capacitance measurements. The time constant is defined as the time it takes for the

capacitor to reach 63.2% of its maximum charge capacity given that it has no initial charge or better to deplete 36.8% of its total charge. Therefore, particles landing in the capacitor channels decrease the total circuit resistance, leading to greater measuring capacitance values for the same time constant. Dicing by means of appropriate dicing tools, after the dielectric paste has been applied, is highly recommended and would prevent particle penetration into the chip channels.

Figure 14. Dicing problems

E. IONIZING RADIATION SOURCE

Cesium is one of the five elemental metals that are liquid at or near room temperature. It can easily bond with chlorides to form a crystalline powder. Cs-137 is its most common radioactive isotope formed by nuclear fission. Cesium has various applications in the medical field, including radiation therapies, gauges, calibration equipment, and medical devices.

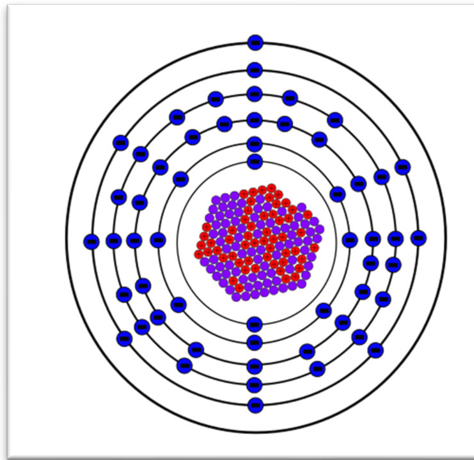

Figure 15. Bohr model of cesium. Source: [24]

A Cs-137 gamma radiation disk was chosen to be used as the ionizing radiation source for testing the dosimeter MEMS sensor. The Cs-137 gamma source disk was bought from Spectrum Techniques. The overall dimensions of the disk were 1.0” x 0.125” and the radioactive material was sealed using epoxy in the bottom of the well of a Plexiglas disk. Sealing with epoxy prevents leakage and contamination from the emitting source, as shown in Figure 16. The gamma radiation emission is achieved without undue absorption through the thin transmission window in the middle of the plastic disk.

Figure 16. Cs-137 gamma radiation disk

The active bead is fixed inside the solid plastic capsule and located at the geometric center of the source.

Energy [keV]	Radionuclide	Transmission factor
47	Pb-210	0.964
60	Am-241	0.958
88	Cd-109	0.970
122	Co-57	0.973
279	Hg-203	0.979
344	Eu-152	0.979
662	Cs-137	0.985
834	Mn-54	0.987
1173	Co-60	0.988
1836	Y-88	0.991

Figure 17. Transmission factors. Source: [25]

According to the manufacturer’s specifications, the Cesium 137 should give a minimum gamma activity of 0.05μCi (1.85 kBq) up to a maximum of 10 μCi (370 kBq), depending on the elapsed time since the manufacturing date. The peak energy of the Cs-137 Radionuclide is 662 keV and the transmission factor is 0.985, as shown in Figure 17. “The transmission factor is the fraction of the gamma-rays produced in the source that will emerge from its surface calculated for narrow beam emission normal to the plane of the source,” as defined by Gammadata Instrument [25]. Moreover, it is obvious that the absorption and scattering effects depend on the experiment set up and therefore on the measurement geometry and the measurement equipment. Table 3 summarizes the most important characteristics of the Cs-137 disk source.

Table 3. Cs-137 disk characteristics

Radionuclide	Cs-137	Units/Equivalent activity
Gamma Energy	662	[keV]
Transmission factor	0.985	
Initial Activity at Calibration	10µCi	(370 kBq)
Activity after 274 days[3]	9.83 µCi	(364 kBq)
Activity after 500 days	9.69 µCi	(359 kBq)
Overall uncertainty	20	[%]
Half-life	30.08	[years]
Overall Diameter	1”	[inches]
Height	0.25”	[inches]
Active Diameter	0.197”	[inches]
Active height	0.125”	[inches]
Manufacturing Date	11 Jan 22	

1. Absorbed Dose

The radiation dose absorbed by the sensor’s dielectric paste was calculated and compared to the evidenced changes of the sensor’s capacitance. Absorbed dose calculations were based on a nominal Cs-137 disk activity. According to the sticker attached to the disk, the radioactive source was manufactured on “11 JAN 2022.”

[3] The experimental procedure occurred approximately 274 days after the manufacturing date.

Considering that Cs-137 has a half-life of 30.08 years the nominal 10μCi radioactivity value was verified using a Geiger-Mueller counter device.

Disk radioactivity:

$$10\mu Ci = 3.7 * 10^5 Bq$$

Therefore, the entire Cs-137 disk gives 370,000 disintegrations per second. By definition, one (1) Becquerel is one decay per second.

Since the original calibrated activity refers to the date of the disk manufacture, the remaining activity could be calculated as follows:

$$R_{Cs-137} = R_{initial} \times exp\,[-\frac{ln(2)}{30.08} \times \left(\frac{days}{365}\right)]$$

where

$$R_{initial} = Original\ calibrated\ Activity$$

and

$$days = Number\ of\ days\ elapsed\ since\ the\ original\ calibrated\ activity\ date.$$

In this study, approximately 274 days had elapsed since calibration; therefore, the estimated remaining activity of the isotope was 9.83μCi.

For the absorbed dose calculations, the following formula was used:

$$P_{source} = R_{Cs-137} \times E_{\gamma} \times 1.60218 \times 10^{-13}$$

$$P_{source} = Power\ of\ ionizing\ radiation\ at\ source\ (Watts)$$

$$R_{Cs-137} = Cs - 137\ radioactivity$$

$$E_{\gamma} = 0.6617\ \text{MeV}\ (\text{Cs} - 137\ \text{peak Energy})$$

For a 10μCi source the radiated power would be

$$P_{source} = 39.2259 \text{ nWatts}$$

where

$$\text{Conversion factor}_{\text{MeV to Watt*seconds}} = 1.60218*10^{-13}.$$

The radiated power from a point source follows the inverse square law, in a similar way the electric field generated by a charge distribution falls off according to Gauss's Law. The emitted photons spread out in space and are intercepted by the MEMS sensor. The power that reaches the MEMS sensor is inversely related to the distance square. The area of the absorbing material, the dielectric of our capacitor, is proportionally related to the dose absorbed by the MEMS sensor.

$$P_{chip} = P_{source} \times T_f \times \frac{1}{4 \times \pi \times d^2} \times A \times \mu \times t$$

$$P_{chip} = Power\ of\ ionizing\ radiation\ absorbed\ by\ the\ chip\ (Watts)$$

$$P_{source} = Power\ of\ ionizing\ radiation\ at\ source\ (Watts)$$

$$T_f = 0.985\ (transmission\ factor)$$

$$d = distance\ from\ gamma\ source\ to\ the\ chip$$

$$A = Surface\ Area\ of\ the\ dielectric\ material^4$$

$$\mu = linear\ attenuation\ coefficient$$

$$t = dielectric\ paste\ thickness$$

The mass attenuation coefficient for PVDF based nanocomposites has been the subject of several studies, with various techniques used to calculate it. Viegas et al. [26] demonstrated an exponential increase in the PVDF mass attenuation coefficient when

[4] Although the MEMS chip is of rectangular shape, the dielectric material applied had a circular cross section as it was applied in a droplet form.

exposed to low photon energies, such as X-Ray photons at 6.9 keV. The same study also found a significant increase in the experimental mass attenuation coefficients for PVDF composites enriched with graphene-based nanocomposites. For photon energies greater than 30 keV, the mass attenuation coefficients were found to be smaller than 1 cm^2/g.

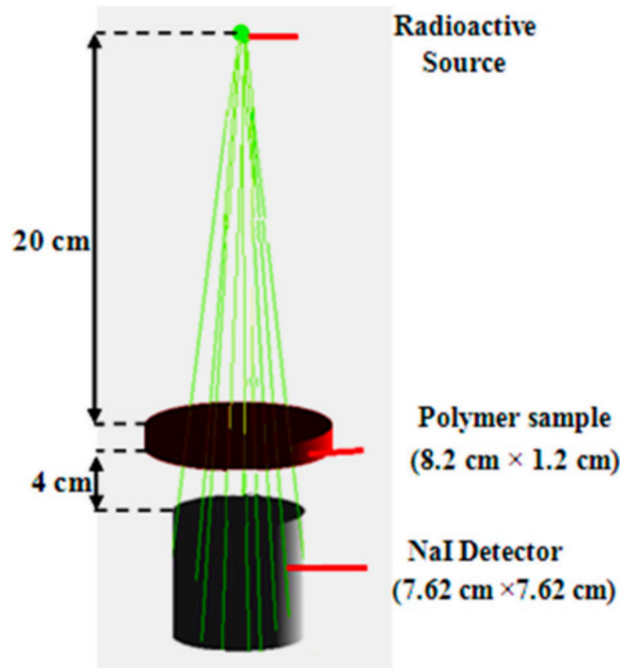

Figure 18. Mass attenuation coefficient calculation set-up. Source: [7]

Similarly, Alabsy et al. [7] showed that PVDF irradiated by a 661.66 keV energy source had a Linear Attenuation Coefficient (μ) of 0.13717 (cm^{-1}) and a Mass Attenuation Coefficient of about 0.07708 (cm^2g^{-1}) .

The total absorbed dose by the dielectric material of the chip sensor can be calculated as follows:

$$AD = \frac{P_{chip} \times TOE}{M_{paste}}$$

$$AD = \text{ absorbed dose in Grays } (Gy)$$

$$P_{chip} = \; Power\ of\ ionizing\ radiation\ absorbed\ by\ the\ chip\ (Watts)$$

$$TOE = time\ of\ exposure\ in\ seconds\ (sec)$$

$$M_{paste} = mass\ of\ the\ dielectric\ paste$$

Or by having all the factors affecting the absorbed dose in one equation:

$$AD = \frac{R_{Cs-137} \times E_{\gamma} \times 1.60218 \times 10^{-13} \times T_f \times A \times \mu \ \times t \times TOE}{M_{paste} \ \times 4 \ \times \pi \ \times d^2}$$

$$AD = absorbed\ dose\ in\ Grays\ (Gy)$$

$$1\,Gy = 1\,J/Kg$$

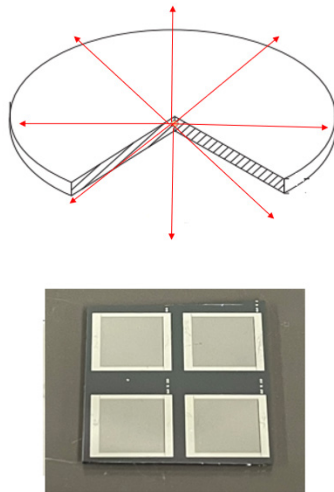

Figure 19. Gamma rays from source to sensor

F. SENSOR CAPACITANCE

In the current research, changes in the capacitance of the MEMS sensors with gamma radiation were recorded and compared to the dose absorbed by the dielectric material. The initial sensor capacitance was both analytically and numerically calculated. For the numerical approach and sensor simulation the COMSOL software was extensively

used. The computed capacitance values were compared to the values collected by means of the available measuring equipment (multimeter, Arduino board and Keysight analyzer).

1. Analytical Calculation of the Sensor Capacitance

For the analytical calculation of the sensor's total capacitance, three (3) different capacitive configurations had to be taken into account.

- Capacitance (C_1): the capacitance between the interdigitated fingers. This is the most important parameter of the study. The channels between the interdigitated fingers are filled with the dielectric material whose properties change with the absorbed radiation dose.

- Capacitance (C_2): the capacitance between the silicon handle layer of the SOI wafer (Figure 2) and the aluminum interdigitated finger electrodes. In this case, it is the Silicon dioxide layer (SiO_2) between the silicon handle layer and the silicon device layer electrode that acts as the dielectric material of the capacitor. The C_2 capacitor would give much greater capacitance values when compared with C_1, because of its larger cross-sectional area.

- Capacitance (C_3): the capacitance between the silicon handle layer and the other silicon device layer electrode including the interdigitated fingers. C_3 capacitance would be exactly equal to C_2 because of symmetry and the same exact C_2 capacitor characteristics.

The three capacitive configurations are connected as shown in Figure 20.

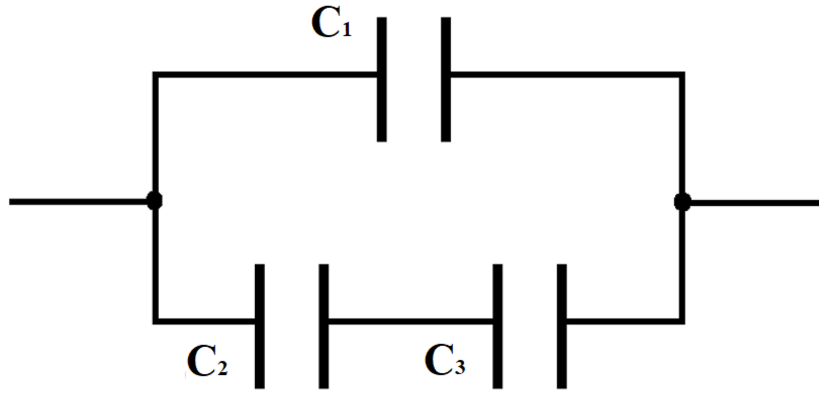

Figure 20. MEMS sensor capacitive configuration

The total capacitance of the MEMS sensor can be calculated as follows:

$$C_{TOT} = C_1 + \frac{C_2 + C_3}{C_2 \times C_3} = C_1 + \frac{C_2 \times C_2}{C_2 + C_3} = C_1 + \frac{C_2}{2}$$

$$C_1 = \varepsilon \times \frac{A_f}{d}$$

where

$$\varepsilon = dielectric\ constant\ of\ sensor\ paste \left(\frac{C^2}{N\,m^2}\right),$$

$$A_f = Total\ Area\ of\ capacitor \frac{fingers}{plates},$$

and

$$d = 20\mu m \left(distance\ between\ the \frac{teeth}{plates}\right).$$

The total area of capacitor fingers (A) can be calculated as

$$A_f = N_{teeth} \times (2 \times L_{tooth} + 2 \times W_{tooth}) \times H_{tooth}.$$

For the 60x20 sensor,

$$N_{teeth} = 60\ (Number\ of\ teeth),$$

$$L_{tooth} = 6.48mm\ (Length\ of\ tooth),$$

$$W_{tooth} = 0.09mm\ (Width\ of\ tooth),$$

and

$$H_{tooth} = 30mm\ (Height\ of\ tooth).$$

Therefore,

$$C_1 = \varepsilon \times (2 \times L_{tooth} + 2 \times W_{tooth}) \times H_{tooth} \times (1/d)$$

For the capacitance between the silicon wafer and the interdigitated finger capacitor we have

$$C_2 = \varepsilon \times \frac{A_w}{d}$$

where

$$\varepsilon = \varepsilon_o\ x\ \varepsilon_r\ (dielectric\ constant\ of\ SiO_2),$$

$$\varepsilon_o = 8.854\ x\ 10^{-12}\ C^2/(N\ m^2),$$

$$\varepsilon_r = SiO_2\ relative\ permitivity\ ^5,$$

$$A_w = N_{teeth} \times (L_{tooth} + W_{tooth}) + A_{pad},$$

and

$$d = 3\mu m\ (thickness\ of\ SiO2\ layer).$$

Therefore, for an "empty" 60x20 MEMS capacitive sensor with a surface area of 26.87 mm^2 having air as the dielectric material

[5] For calculation of the SiO_2 capacitance an ε_r value of 2-2.35 has been considered. Values of 3.7-3.9 have also been reported [27]

$$C_{1air} = 10.47\text{pF}$$

and

$$C_{2SiO2} = 93.18\text{pF}.$$

Thus,

$$C_{TOTair} = 103.58 \text{ pF}.$$

For the same MEMS capacitive sensor using pure PVDF as the dielectric material,

$$C_{1pvdf} = 41.62pF^{6}.$$

$$C_{2SiO2} = 93.18\text{pF}$$

C_2 does not change, as it is again the Silicon Dioxide layer that acts as the dielectric material.

Moreover, and for this particular case, the pure PVDF used as a dielectric was not applied over the whole surface of the MEMS chip and paste penetration to full depth cannot be implied. Therefore, ε_r was estimated around 4 [28].

Thus,

$$C_{TOTpvdf} = 134.88 \text{ pF}.$$

2. Numerical Calculation of the Sensor Capacitance

Another numerical calculation of the sensor's total capacitance has been performed by the COMSOL software. It has been used for the simulation of the MEMS sensor and its capacitance.

[6] For the PVDF, εr varies based on phase and frequency. Moreover, the PVDF dielectric paste does not fully cover the chip's surface and penetration to full depth cannot be assumed. Therefore, an average εr factor of 4 has been considered.

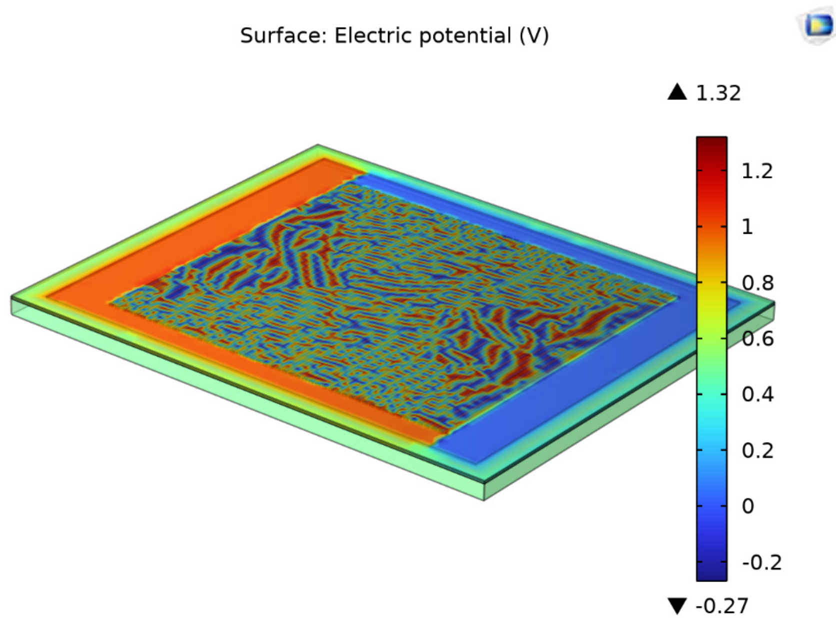

Figure 21. 60x20 MEMS sensor simulation by using COMSOL.

For a 30x20 MEMS capacitive sensor using air as the dielectric material the following results were retrieved.

Sensor surface area:

$$A_{sensor} = 0.3039\ cm^2$$

Sensor capacitance values:

$$C_{1air} = 8.5065\ pF$$

$$C_2 = 214.99\text{pF}$$

Thus,

$$C_{TOTair} = 118.28\ \text{pF}.$$

For a 60x20 MEMS capacitive sensor using air as the dielectric material the following results were retrieved:

Sensor surface area:

$$A_{sensor} = 0.2687\ cm^2$$

Sensor capacitance values:

$$C_{1air} = 16.397\text{pF}$$

$$C_2 = \ 282.25\ \text{pF}$$

$$C_{TOTair} = \ 150.71\ \text{pF}$$

3. Measuring the Sensor Capacitance

As a final step the sensor capacitance was measured by means of three different equipment. Measurements received from the Arduino Board, the Keysight testing device, and the Elenco multimeter have been collected and compared with the values obtained by the numerical and analytical methods, as shown in Figure 22.

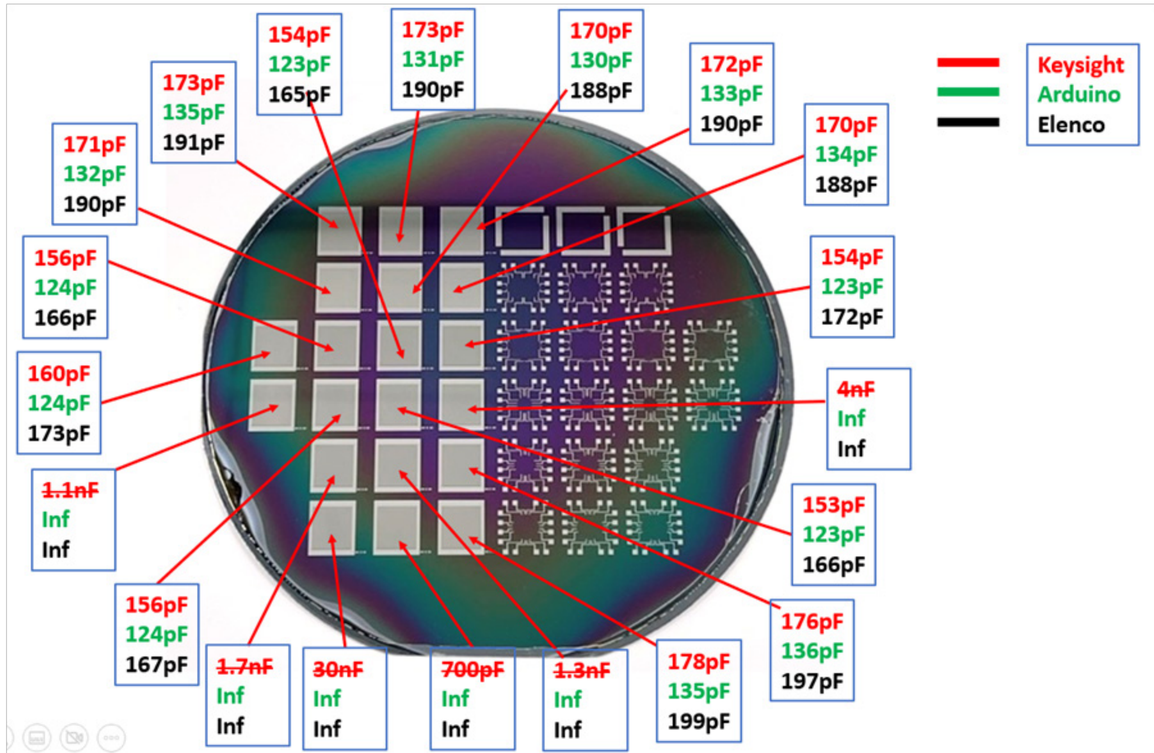

Figure 22. MEMS capacitors and their recorded capacitance values

4. Results Comparison

In this section, a summary of the capacitance values for a 60x20 MEMS sensor is provided for comparison between the different measuring methods used in this thesis. The numerically and analytically calculated values along with the measurements obtained by means of the three measuring methods are shown in Table 4. It is important to note that the analytical and numerical calculation of the sensor's total capacitance assumes ideal conditions, including perfect alignment of the interdigitated fingers and uniform dielectric properties throughout the dielectric material. However, in reality, imperfections in the sensor fabrication process and non-uniform radiation dose distribution can lead to deviations from the calculated capacitance values. The MEMS sensor geometrical features are also included in Table 3. It is evident that the accuracy and the precision of the measuring devices greatly affect the recorded capacitance values. Moreover, numerical calculations take into consideration multiple parameters and therefore the capacitance values obtained using COMSOL seem to be much more accurate when compared to the

simple analytical calculations described in Section 1. The Keysight analyzer is a high precision device and therefore some deviation from the results derived by COMSOL is justified. As expected, the values calculated numerically are much closer to the measured capacitance values.

Table 4. Capacitance values for an "empty" 60x20 MEMS sensor

	Description	**Values**	**Units**
Capacitance	Arduino	123	pF
	Keysight	153	pF
	Elenco	165	pF
	Numerical	150.71	pF
	Analytical	103.58	pF
Chip/Wafer Characteristics	Surface area	0.2687	cm^2
	SiO_2 dielectric constant	2-2.35	
	SiO_2 thickness	3	μm
Interdigitated fingers Characteristics	Number of fingers	60	
	Length	6.48	mm
	Width	0.09	mm
	Thickness	30	mm
	Separating distance	20	μm

It is important to note that despite the significant differences among the obtained capacitance values using different measuring platforms, the selection of the measuring platform would not affect the reliability of the experimental outcomes. This is because the

primary factor of the investigation was the capacitance change with the radiation absorbed dose and defining radiation effects with absorbed dose only required capacitance change tracking. Therefore, Table 4 is provided for reference purposes only.

THIS PAGE INTENTIONALLY LEFT BLANK

IV. EXPERIMENTAL RESULTS

In this chapter, the results collected during the exposure of the MEMS capacitive sensors with different dielectrics to a Cs-137 disk source are presented, following Benjamin P. McHale's [23] suggestion for further research. The interdigitated finger design of the fabricated MEMS sensors was successfully deployed for measuring the ionizing radiation absorbed dose. PVDF was the primary component for both dielectric pastes used for the fabrication of the capacitive sensors, and pure PVDF and PVDF-carbon black composite pastes showed similar behavior when exposed to gamma radiation. A significant increase in the sensor capacitance with the absorbed dose has been observed as a result of the incurring chemical ageing effects.

A. PURE PVDF MEMS SENSOR

1. Sensor Irradiation

Before exposing the MEMS sensor to the gamma radiation source, its initial capacitance was determined by performing a series of measurements using different methods for cross reference. Three different measuring devices were used for this purpose, namely a Keysight analyzer device, an Arduino board and an Elenco multimeter, as shown in Figure 23. The script used for the Arduino ELEGOO MEGA 2560 Board can be found in Appendix A. The capacitance of the MEMS sensor was measured by the Arduino platform, which recorded the time it took for the interdigitated capacitor to reach 63.2% of its voltage when fully charged and divided it by the circuit resistance value as defined by the user. The initial reference capacitance value was determined to be 153 pF. Any deviations in the recorded capacitance values were attributed to differences in the devices' characteristics such as circuit resistance, device precision and tolerance and electronic noise in any of the measurement components. The wiring and parasitic capacitance could also have played a role depending on the measuring configuration. The Arduino measuring platform was preferred over all other methods for its portability and its continuous real-time measurements and recordings. The behavior of the sensors was monitored for a significant time period before exposure to the gamma radiation source to establish the

measurement baseline. Once a steady capacitance value was observed, the radiation source was mounted on top of the clamshell box. The radiation dose absorbed by the MEMS sensor dielectric material was estimated using the formulas in Chapter III. The measuring platform would perform one (1) measurement every two (2) seconds; therefore, the total time of exposure was calculated based on the total number of measurements recorded.

Following a fifteen-day exposure, the radiation-induced effects on the capacitance of the pure PVDF sensor were recorded and analyzed. Raw measurements as collected by the Arduino measuring platform can be seen in Figure 23. A total of 677,997 measurements were recorded. The total absorbed dose was estimated at 28.46 mGy.

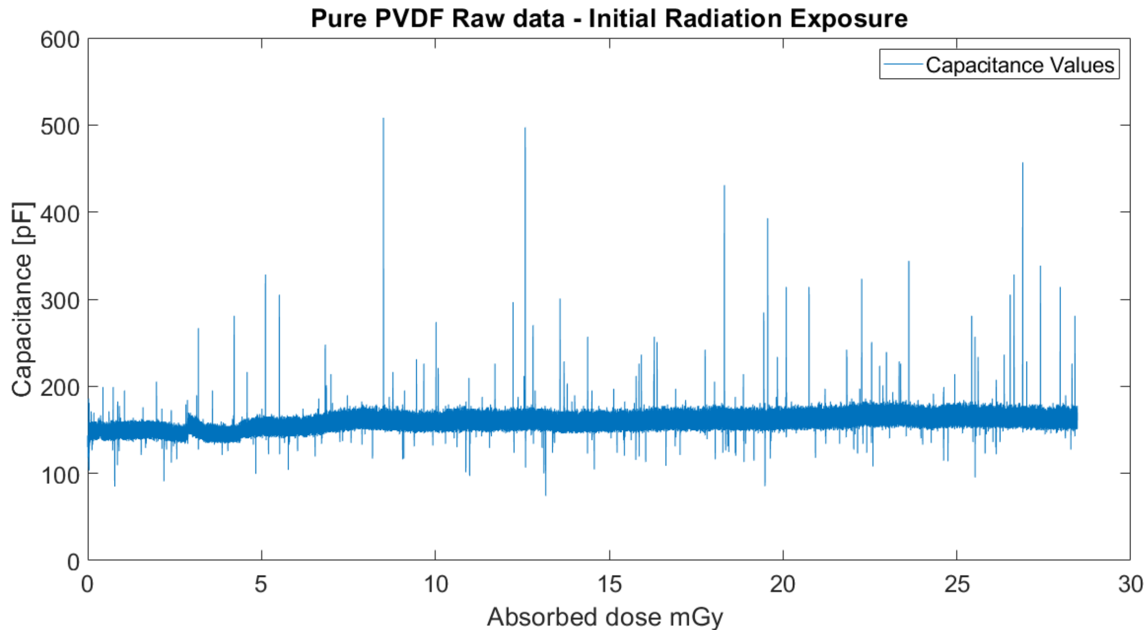

Figure 23. PVDF sensor raw capacitance data

Like the photodetection process, radiation detection involves the interaction of discrete photons with valence electrons. Due to the discrete nature of the photons, there is a randomness in their arrival, which leads to unavoidable fluctuations. As a result, quantum noise is one of the factors that may affect the observed values. In addition, the aluminum structure of the capacitor and its contact with the copper pins of the chip test shell act as resistors of the MEMS sensor circuitry. Thermal noise, or Johnson noise, in the form of

voltage fluctuations across the resistor structure due to random motions of the conduction electrons [29] obviously affects the capacitance measurements. Thermal noise can lead to weak signals being drowned out and can limit the sensitivity of the MEMS sensors. Temperature control of the sensor could improve both precision and sensitivity, as thermal noise increases with temperature.

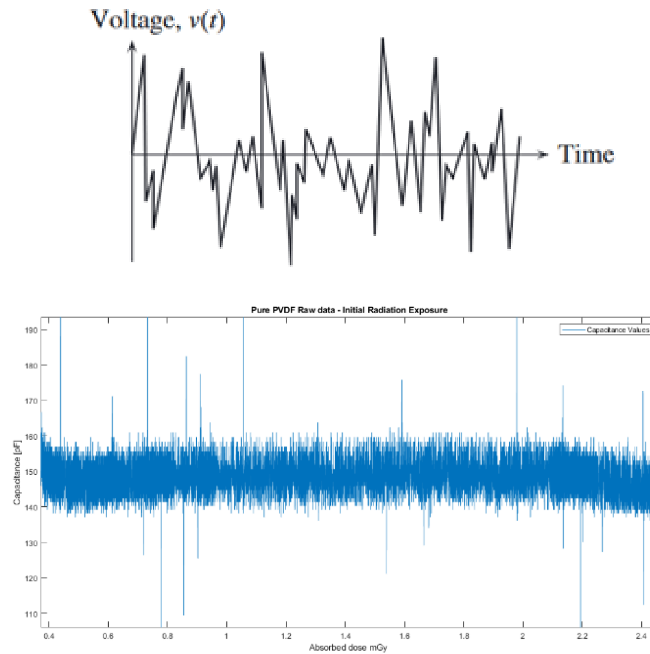

Figure 24. Noise in measurements. Random motion of conduction electrons in a conductor, resulting in electrical noise (top). Source: [29]. Experimental capacitance measurements (bottom)

For appropriate interpretation of the radiation-induced effects, several data-analysis techniques were applied over the recorded raw data. Due to the large number of measurements, further data processing was necessary to draw reliable conclusions. Outliners observed in Figure 24 could have a strong effect on the data analysis, so they had to be eliminated or significantly reduced before proceeding.

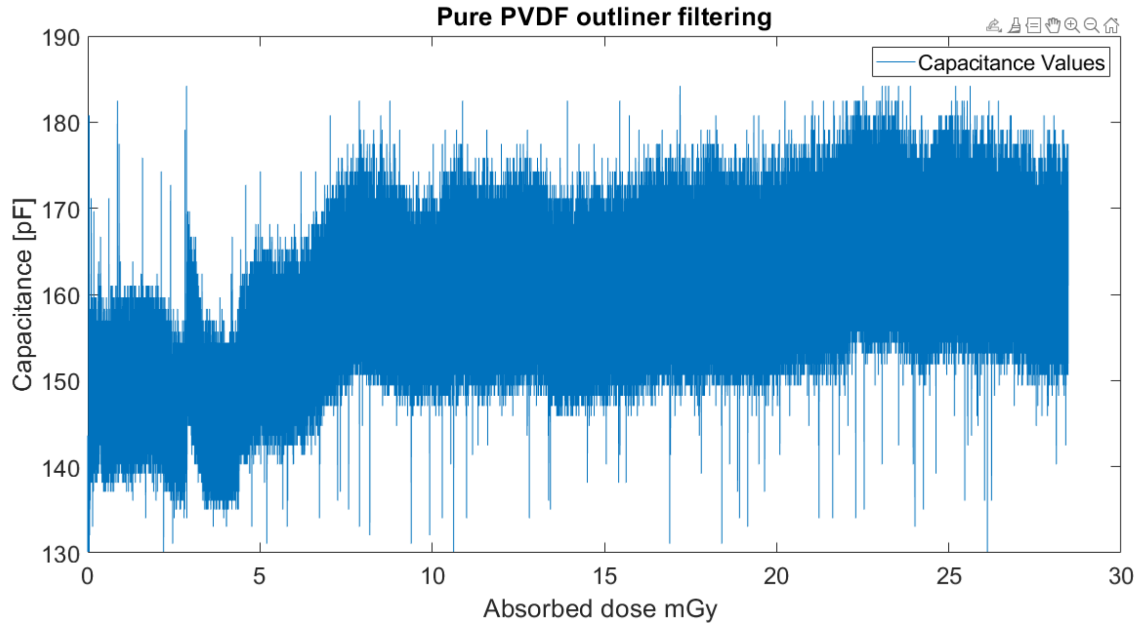

Figure 25. PVDF sensor outliners filtering

Following a significant reduction in outliners, as shown in Figure 25, there were strong indications of an increase in capacitance with the absorbed radiation dose. It should be noted that the high peak of capacitance for an absorbed dose of approximately 3.5 mGy was attributed to power-related issues and should not be regarded as a radiation-induced effect. Figure 26 shows the average capacitance value per hour of exposure, and it is evident that the absorbed radiation dose has a positive effect on the sensor capacitance.

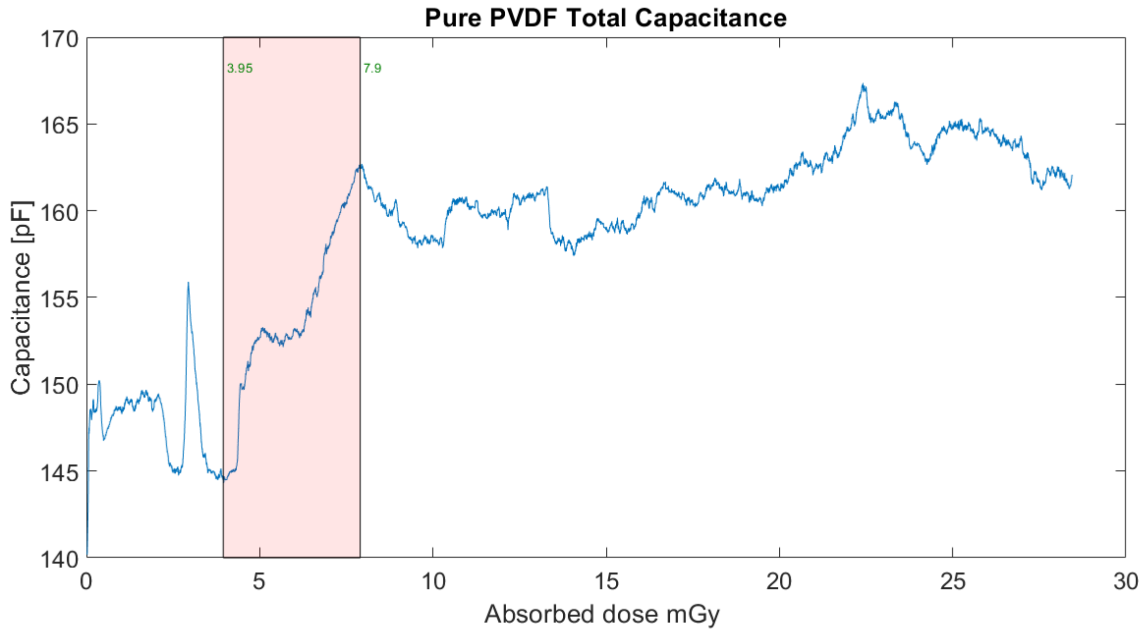

Figure 26. PVDF sensor total capacitance versus absorbed dose

As shown in Figure 26, irradiating the MEMS sensor with doses ranging from 3.95 to 7.9 mGy resulted in a significant increase in the total sensor capacitance values. To better understand the radiation-induced effects on the sensor capacitance, the unwanted electrode-to-handle-wafer capacitance value was subtracted. A value of 112 pF for the electrode to handle wafer capacitance was estimated for the 60x20 sensor by using the COMSOL software, after adjusting the values to the Arduino measurements. However, it should be noted that the theoretically and the numerically calculated values may significantly differ from the actual values, due to undercuts, impurities or other factors related to the fabrication process.

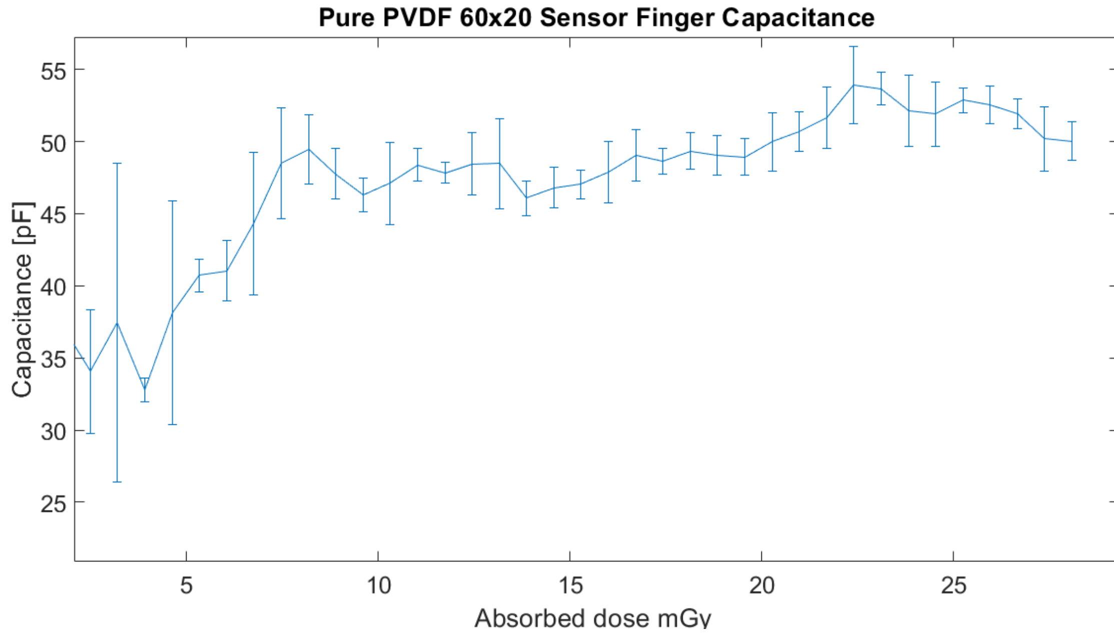

Figure 27. PVDF sensor finger capacitance vs. absorbed dose

An average value of 38 pF was estimated for the interdigitated fingers-PVDF capacitor by subtracting the unwanted electrode-to-handle-wafer capacitance. Using the COMSOL software, a value of 16.17 pF was estimated for the empty interdigitated finger capacitor. It should be noted that the dielectric constant strongly depends on the PVDF crystal phases, which are identified as α, β, γ, and δ, and therefore different phases would yield different dielectric constants. The dielectric constant of 2.35 was estimated for the PVDF dielectric paste, assuming an initial value of 38 pF. The finger capacitance value reached a maximum of 55.36 pF. Figure 28 shows the percentile changes in capacitance.

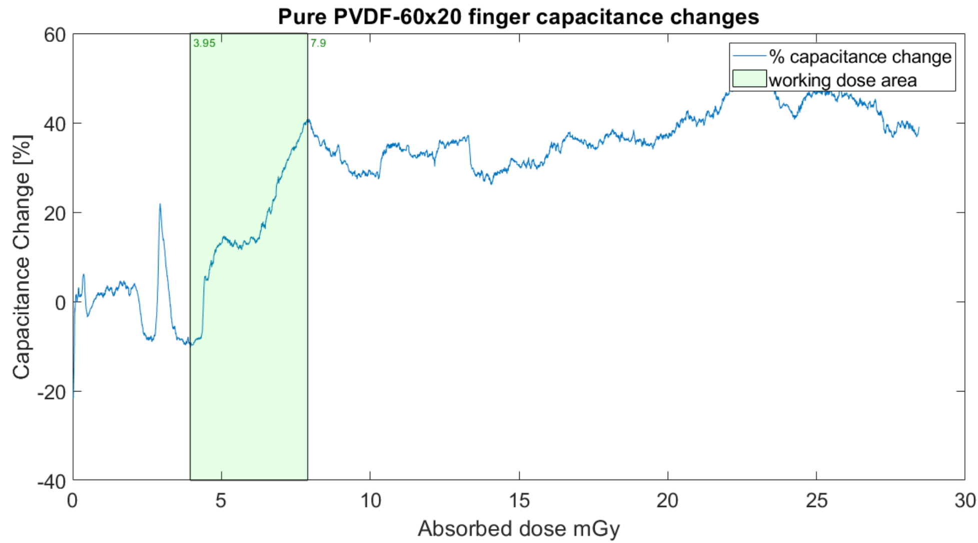

Figure 28. PVDF sensor finger capacitance changes

A significant increase in capacitance was observed with the absorbed radiation dose for doses greater than 3.95 mGy. The maximum recorded increase in sensor finger capacitance was 53.78% and 40.8% for the working area. An average increase of 45% was estimated for doses greater than 7.86 mGy. The increase in capacitance can be attributed to an increase in the dielectric constant of the PVDF paste due to the effects of gamma radiation on the depolymerization of the paste. Consequently, the dielectric constant of the PVDF paste increased from 2.35 to 3.41, a 45% increase.

Although irradiation of the MEMS sensor with doses form 3.95 mGy to 7.86 mGy caused a considerable increase in the capacitance values , the percentage change was not as great as in similar studies [9] , [4]. The application of the dielectric paste over the sensor surface did not cover its total cross-sectional area and probably did not penetrate the channels between the interdigitated finger to the fullest extent, which may have influenced the capacitance change observations. Better control of the insertion of the dielectric mix between the interdigitated fingers could be an area of future work that would enable the fabrication of higher sensitivity sensors.

2. Sensor Annealing

Resetting capabilities to their initial nominal capacitance values would be necessary for re-usable MEMS sensors. To achieve this, annealing of the dielectric paste was investigated, which involved baking the MEMS sensor at 170º C for 10 minutes. After the annealing process, a lower sensor capacitance was observed, and a nominal capacitance value of 87.66 pF was measured, as shown in Figure 29. A total of 42,533 measurements were recorded over a one-day period.

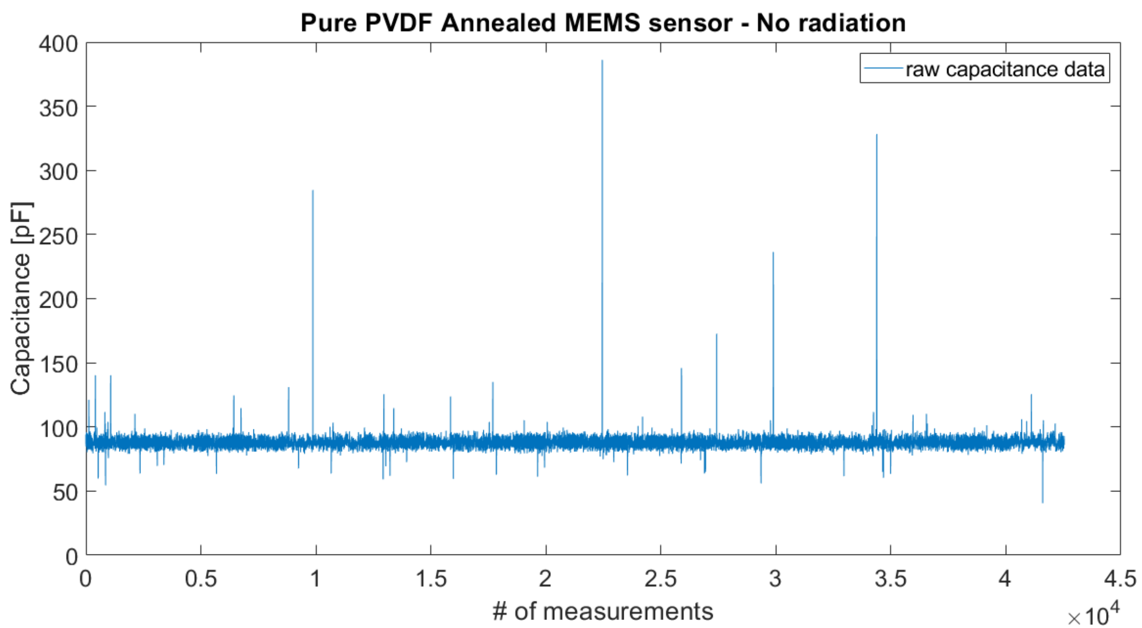

Figure 29. 60x20 MEMS sensor capacitance after annealing

After eliminating the outliners and processing the collected data, a mean capacitance value of 87.66 pF was obtained, as shown in Figures 30 and 31.

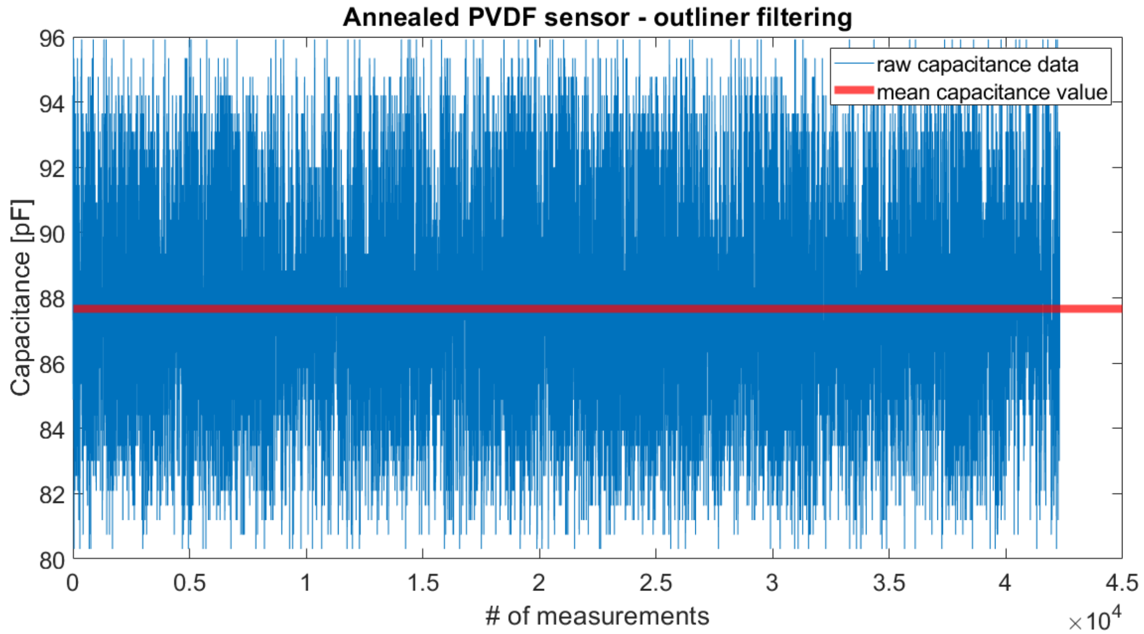

Figure 30. Outliner filtering after sensor annealing

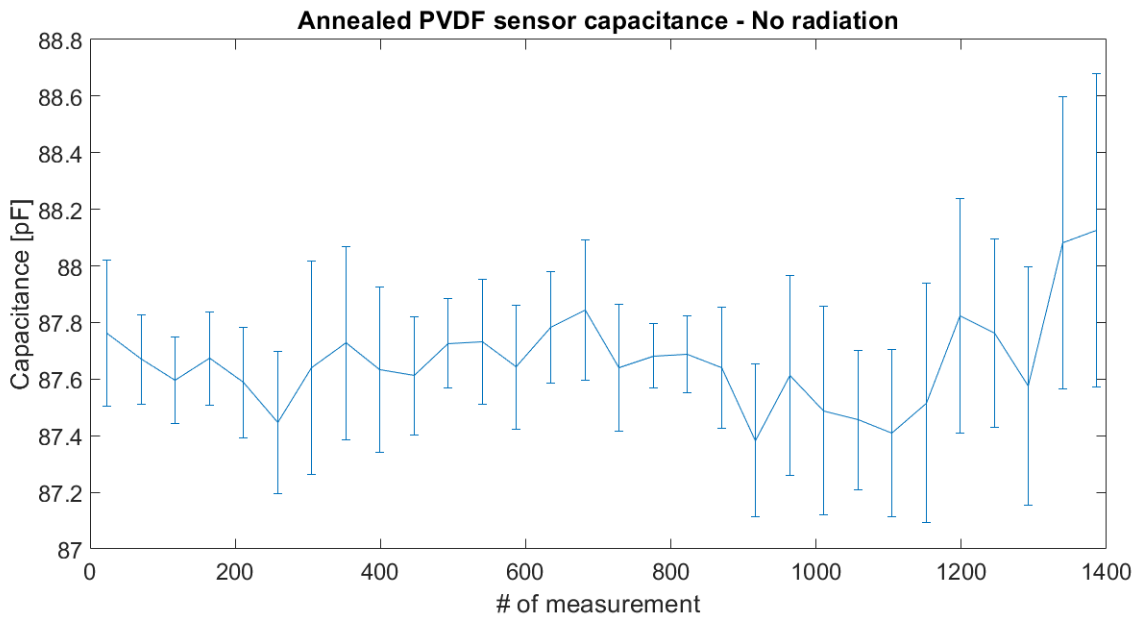

Figure 31. Annealed sensor capacitance

Following the acquisition of the capacitance baseline for the annealed sensor, a new irradiation cycle was initiated. Figures 32 and 33 illustrate the behavior of the sensor during a brief radiation exposure of approximately 12 hours.

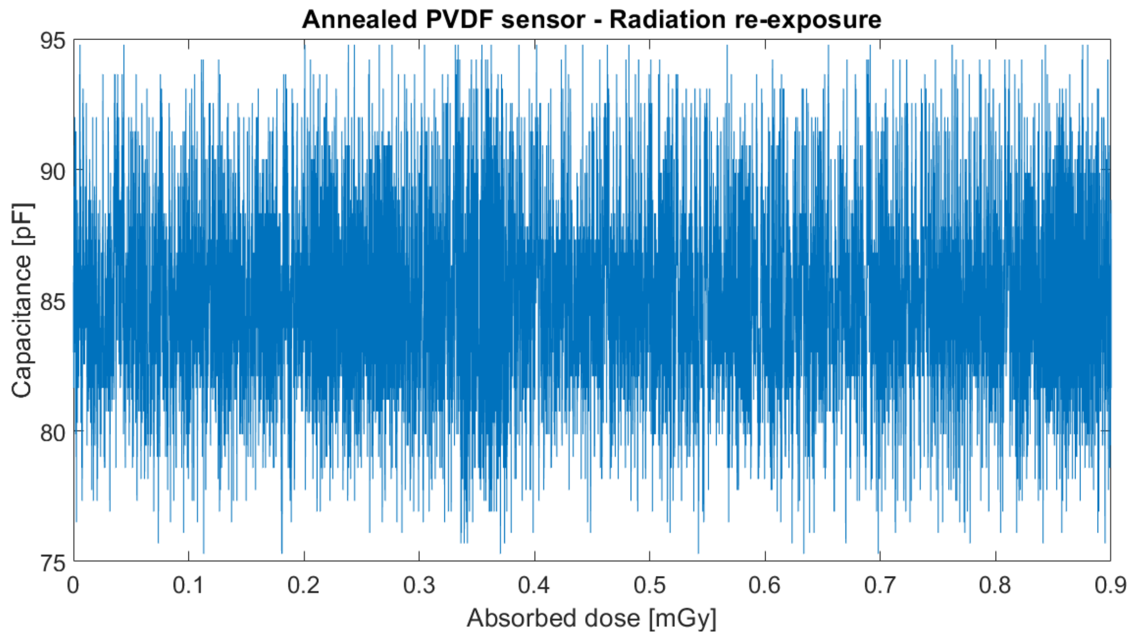

Figure 32. Annealed PVDF sensor irradiation

No significant radiation induced effects were observed during the 12-hour exposure, as depicted in Figure 33.

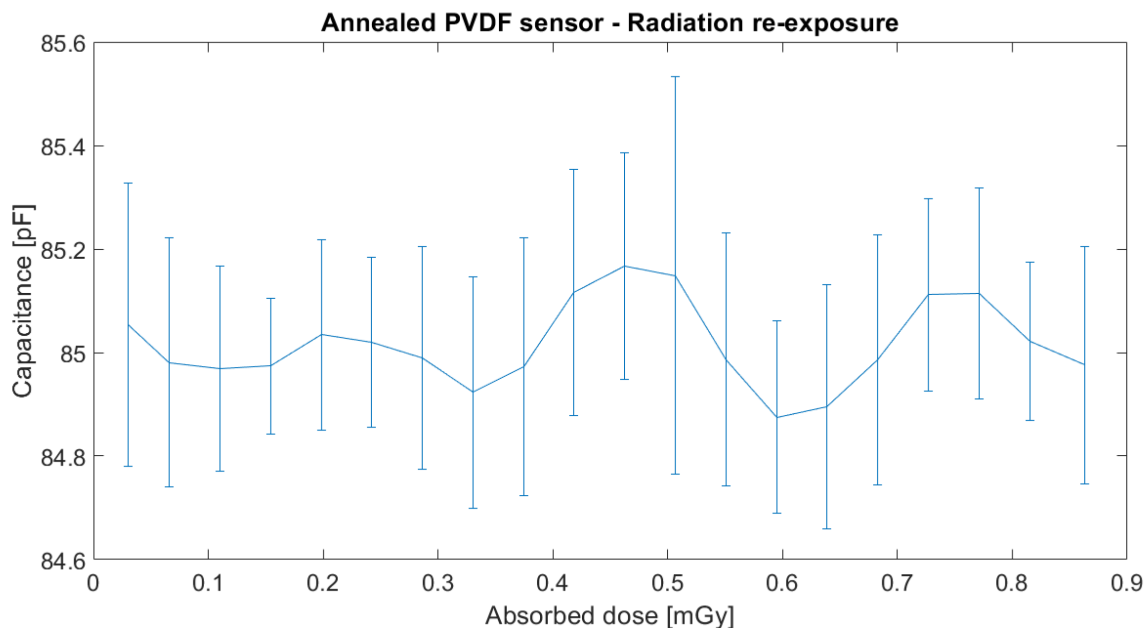

Figure 33. Capacitance measurements for the annealed sensor

No significant capacitance changes were observed even after continuing the irradiation of the annealed PVDF sensor for five (5) more days. Furthermore, after a 7-day period of exposure, no radiation-induced effects on the sensor's capacitance were observed. As shown in Figure 34, the estimated average capacitance was 85.076 pF, and fluctuations of about 4% due to noise in the recorded measurements were also observed. It should be noted that the slight difference between the average capacitance values shown in figures 33 and 34 was attributed to the chip removal and re-installation in the clamshell box.

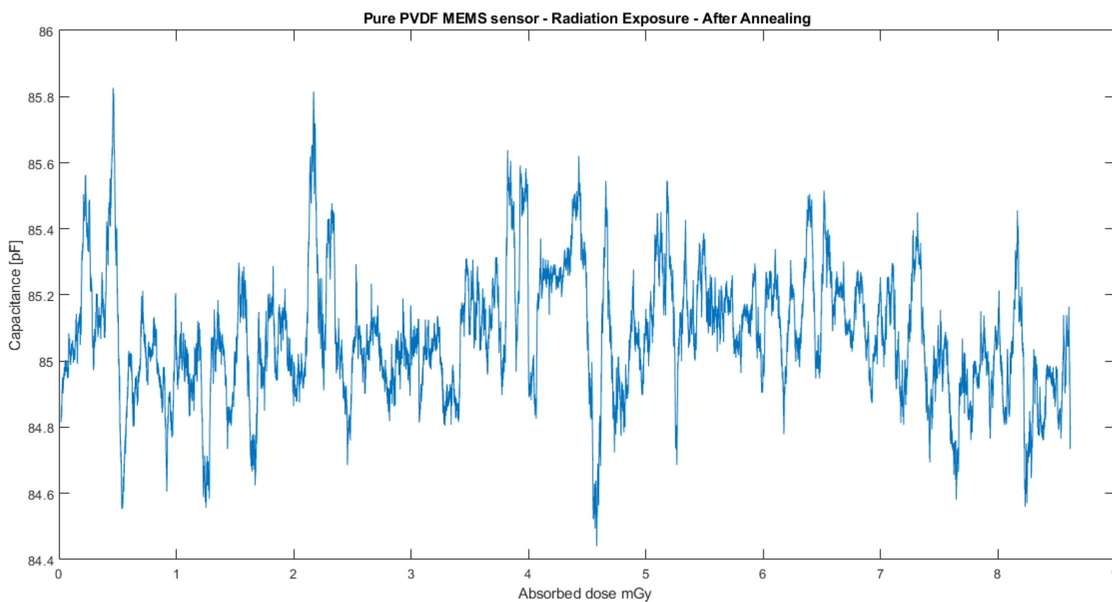

Figure 34. PVDF sensor capacitance – 7-day re-exposure after annealing

After exposing the annealed MEMS sensor to gamma radiation for seven (7) days no significant capacitance changes were observed. However, it is important to note that the annealing at 170ºC may have caused damage to the sensor's structure, making it difficult to draw definitive conclusions. Further research is needed to determine the optimal temperature and duration for sensor annealing.

It is important to consider that the dielectric properties of the PVDF paste are strongly influenced by its crystal phase. The polarity of the PVDF molecules is affected by the crystal structure, resulting in different dielectric constants for PVDF pastes with

different crystal phases. The high temperature annealing process likely altered the PVDF's crystal structure, leading to a lower dielectric constant. A lower annealing temperature followed by a quenching at 20º C may lead to better crystallinity and improved dielectric constant values, particularly for the β phase of PVDF, which is most desirable for MEMS sensors [30].

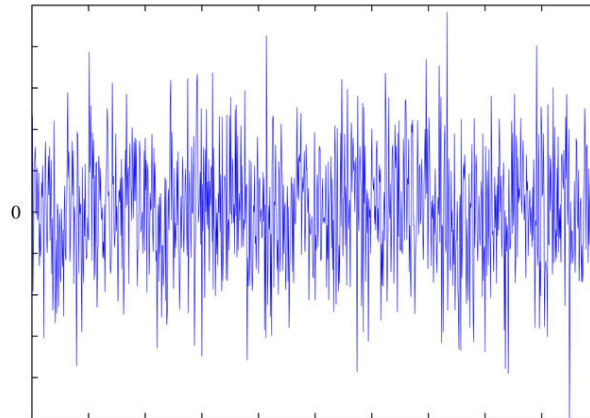

Figure 35. White noise. Source: [31]

B. C-PVDF MEMS SENSOR

Similar steps were followed for the analysis of the radiation induced effects over a C-PVDF MEMS sensor. The sensor's nominal capacitance value obtained was 128.4 pF. A total of 926,296 capacitance measurements were recorded over a period of 21 days. The total absorbed dose was estimated at 38.88 mGy. The capacitance values as recorded by the measuring platform are shown in Figure 36.

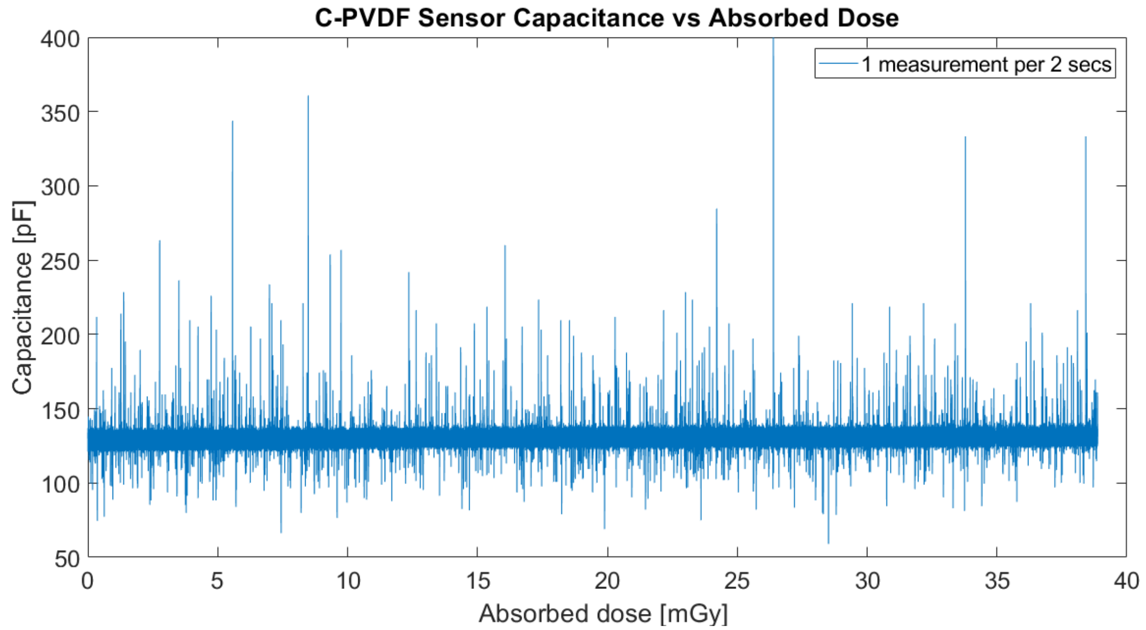

Figure 36. C-PVDF sensor raw capacitance data

As shown in Figure 36, the presence of carbon particles has a significant impact on the measurement noise. Despite applying the C-PVDF paste on a MEMS sensor with similar geometry and structure to the pure PVDF MEMS sensor, the capacitance outputs exhibit more frequent and intense fluctuations. This is because carbon particles increase the random motion of the conduction electrons, leading to higher thermal noise in the circuit.

As shown in Figure 37 the outliners were filtered out by means of filtering techniques, so that they don't affect the interpretation of the results.

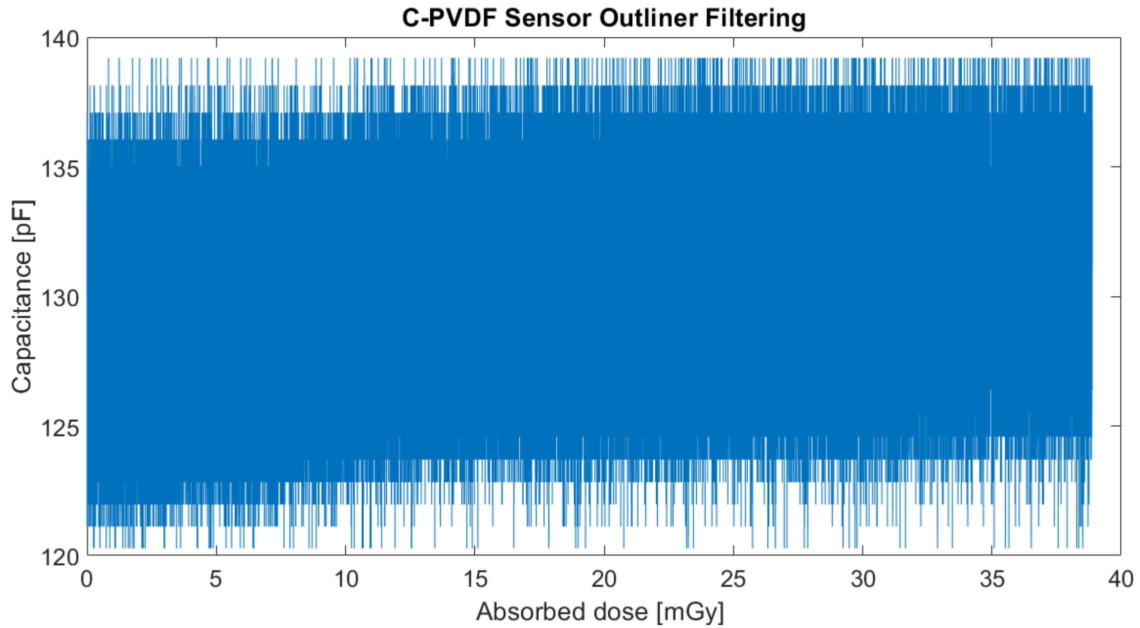

Figure 37. C-PVDF sensor outliners filtering

It is evident that carbon loading results in an increased conductivity of the dielectric paste when compared to the pure PVDF sensor. However, by keeping the carbon composite lower than 1%, its capacitance can still be used as a good indicator to trace the effects of gamma radiation on a MEMS sensor. It is expected that carbon loading will decrease the sensor capacitance and consequently, any observed changes might not be as intense as in the case of the pure PVDF sensor. Following the outliner filtering process, as described in the previous sections, the average capacitance value per hour of exposure is shown in Figure 38.

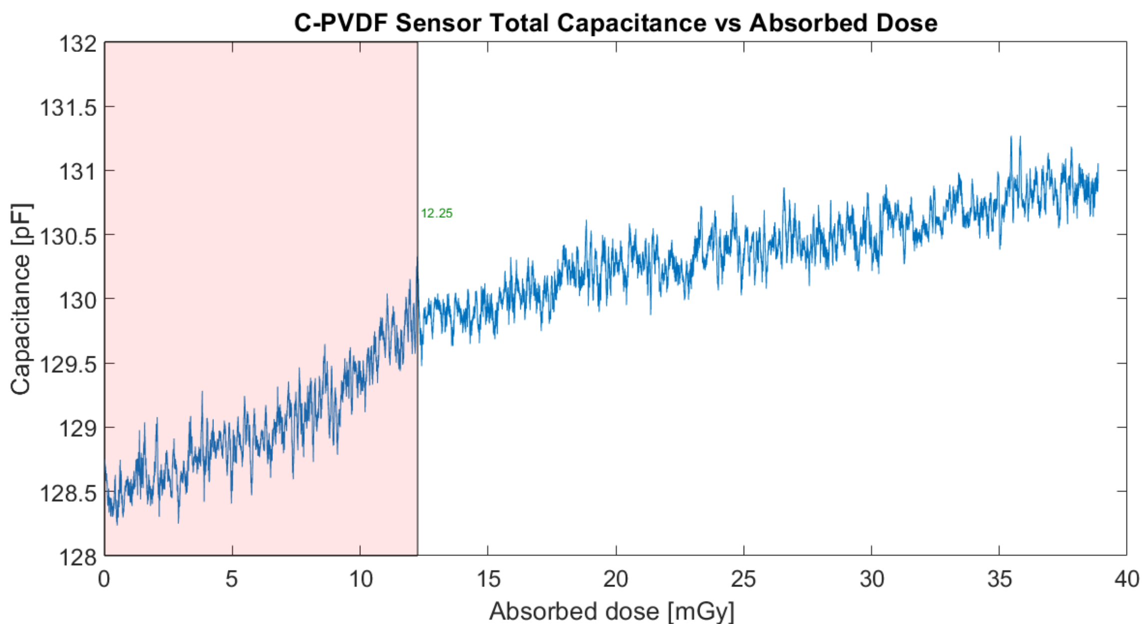

Figure 38. C-PVDF sensor total capacitance

As shown in Figure 38, the addition of carbon particles in the PVDF dielectric paste led to an immediate increase in the capacitance values with the absorbed dose. It can be inferred that carbon composites can be used to reduce the sensor's working dose without any waiting depolymerization period. Furthermore, a less steep increase in capacitance with absorbed dose was observed. It is probable that the addition of carbon allowed for a much more uniform depolymerization process throughout the dielectric paste.

To better understand the radiation induced effects, the value of the unwanted electrode-to-handle wafer capacitance was subtracted. The electrode-to-handle wafer capacitance value of 109 pF was estimated for the 30x20 sensor by using the COMSOL software and adjusting the values to the Arduino measurements.

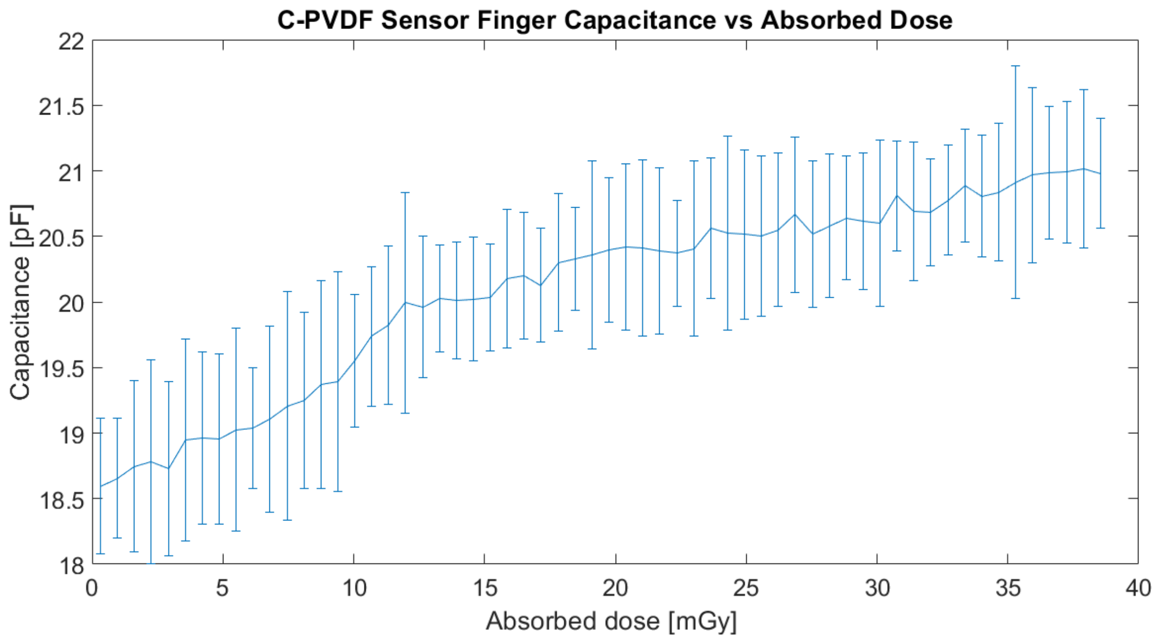

Figure 39. C-PVDF sensor finger capacitance

By subtracting the value of the unwanted electrode to handle wafer capacitance, an average value of 18.5 pF was obtained for the C-PVDF—interdigitated finger capacitor (C_1). Using the same procedure as described in the previous sections and the COMSOL software, a dielectric constant of two (2) was estimated for the C-PVDF dielectric paste. As shown in Figure 39, the capacitance values followed an almost linear increase with the absorbed dose. By the end of the radiation exposure, a total capacitance increase of 14.7%. was observed, with the absolute finger capacitance increasing from an initial low of 18.5pF up to a final high of 21.22 pF. The percentage capacitance changes along with the sensor working area are shown in Figure 40.

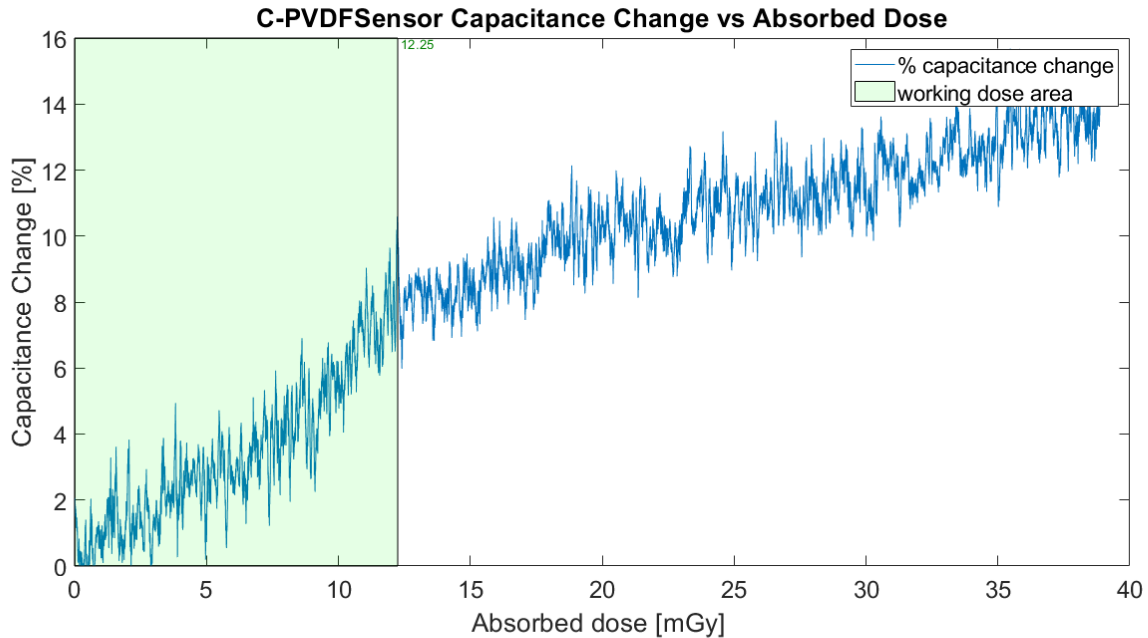

Figure 40. C-PVDF sensor finger capacitance changes

An immediate increase in capacitance with the absorbed dose was observed for the C-PVDF sensor. Although a decrease in the capacitance change rate was observed after a dose of 12.25 mGy, no capacitance plateau was reached even after a period of twentyone (21) days and a total absorbed dose of 38.8 mGy. The C-PVDF sensor showed a linear response to a working dose from 0 to 9.59 mGy. By the end of the exposure, a maximum increase in finger capacitance of 14.7% was observed. Similar to the pure PVDF sensor, the increase in capacitance can be attributed to an increase in its dielectric constant of the C-PVDF paste. Therefore, the dielectric constant of the C-PVDF paste increased from an initial value of 2 to a final value of 2.3, indicating a 15% increase.

C. PVDF VERSUS C-PVDF MEMS SENSOR

By comparing the radiation induced effects imposed on the two MEMS sensors, useful observations can be made. Figure 41 shows the percentile changes in the finger capacitance with absorbed dose for the PVDF and the C-PVDF MEMS sensors.

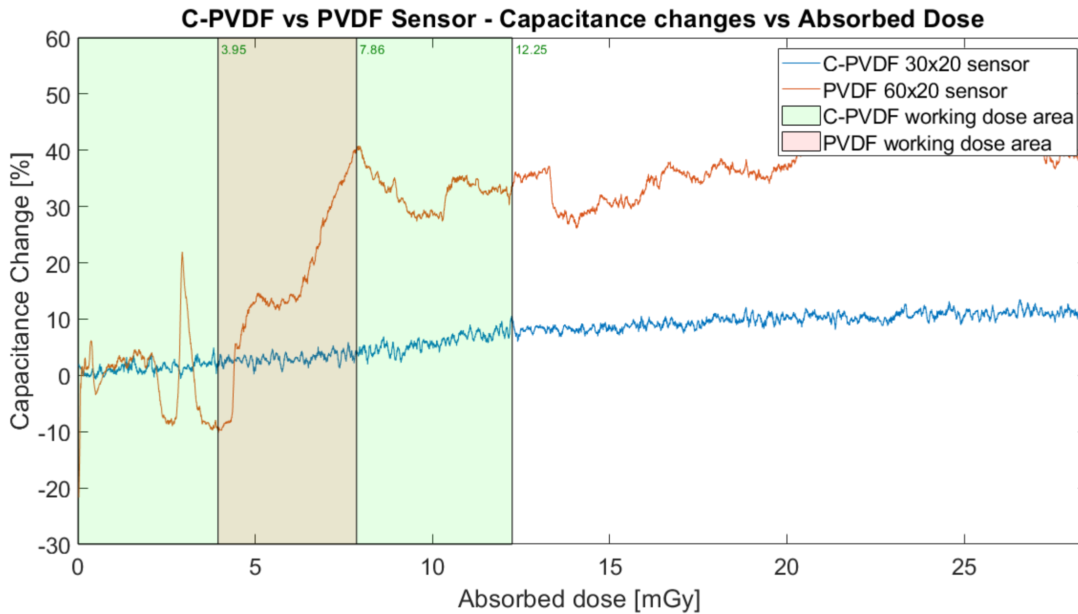

Figure 41. C-PVDF versus PVDF sensor comparison

The pure PVDF sensor showed an average capacitance increase of 45% while the C-PVDF showed a smaller increase of 15% over a longer period of exposure. Although carbon particles can aid in the depolymerization of the PVDF paste, their higher conductivity also lowers the capacitance values. As the dielectric paste contains polar molecules, they will generally be in random orientations when no electric field is applied. An applied electric field will polarize the material by orienting the dipole moments of polar molecules. Although PVDF is a good insulator, the presence of the carbon particles increases the effective electric field between the plates and reduces the capacitance of the parallel plate finger structure. Furthermore, the fabrication of the C-PVDF sensor required a smaller amount of PVDF as more solvent was needed for a homogeneous mixture. While the addition of carbon black likely accelerated the depolymerization of the PVDF, resulting

in enhanced chemical aging processes such as chain scission, the decreased amount of PVDF used in the C-PVDF sensor led to a lower total sensor capacitance and less intense capacitance changes due to radiation-induced effects.

Finally, the C-PVDF sensor showed a much more linear behavior when compared to the pure PVDF sensor. The PVDF sensor, on the other hand, showed a considerable and abrupt increase in capacitance values for irradiation doses between 3.95 and 7.9 mGy. The dielectric constants increased from 2.35 to 3.41 and from 2 to 2.3 for the pure PVDF and the C-PVDF sensor pastes respectively.

A summary of the results can be found in Table 5.

Table 5. PVDF and C-PVDF results summary

	PVDF	**C-PVDF**
Nominal Capacitance (pF)	153	128.4
Initial Dielectric Constant	2.35	2
Final Dielectric Constant	3.41	2.3
Increase in Capacitance (%)	45	15
Days of Exposure	15	21
Absorbed dose (mGy)	27	38
Working dose (mGy)	3.95–7.96	0–9.59

THIS PAGE INTENTIONALLY LEFT BLANK

V. CONCLUSIONS AND FUTURE WORK

A. CONCLUSIONS

The goal of this thesis was to utilize MEMS technology to develop a cost-effective miniaturized sensor for gamma radiation dosimetry applications. Two different sensors were fabricated and deployed for radiation dose measurements, with the minimum detectable radiation dose and the radiation dose working range being the most critical parameters to consider for the sensors under investigation. The absorbed radiation dose was successfully correlated with the sensor responses. The thesis research revealed that controlling the composites of their dielectric pastes can produce different sensor responses.

The choice of PVDF as the main ingredient in the dielectric paste composites was based on previous research. The chemical ageing of the PVDF paste, which leads to depolymerization through chain scission, resulted in increased dielectric constants, and consequently, greater capacitance values for both the pure PVDF and the C-PVDF sensors. By controlling the mixing rates of the dielectric paste composites, it is possible to achieve a controlled sensor behavior. The C-PVDF sensor demonstrated a faster response, broader radiation dose working range, and a much more linear behavior compared to the pure PVDF sensor. However, the pure PVDF sensor showed a greater capacitance increase within a narrower working range, which may be advantageous in high sensitivity, low dose applications. It is evident that a controlled sensor behavior can be achieved by combining different mixing ratios of the dielectric paste composites.

Using the same principle, a "nose" radiation detector could be created by combining materials susceptible to different types of ionizing radiation. MEMS technology enables the fabrication of miniaturized sensors, allowing for separate sensing elements to be stacked together to form the "nose" sensor. A compound sensor for the detection and the identification of fissile materials used on nuclear weapons or other sources of ionizing radiation could be built by using a combination of gamma and neutron radiation sensitive materials. Researching and identifying materials whose properties change with exposure

to radiation sources could enable the fabrication of a “nose” sensor with enhanced and multilateral sensing capabilities.

Following the successful deployment of the MEMS sensors for the detection of gamma radiation sources, along with the measurement of the absorbed radiation dose, it seems feasible to integrate them into small portable electronic devices. The MEMS sensor could be powered from an electronic device, such as a smartphone, and a mobile app could be used for the analysis of the collected data. Additionally, radiation-related information could be displayed on the user’s screen. While a reusable sensor via annealing techniques was not identified in this thesis, the low cost of the MEMS sensor allows for its inexpensive replacement after reaching the absorbed dose limit. In general, annealing techniques may require high temperatures, and therefore, real-time and on-site sensor annealing might not always be possible. In such cases, replacing the radiation-affected sensors would be unavoidable.

B. FUTURE WORK

The fabrication of reusable sensors requires further investigation into appropriate annealing techniques that can reset the dielectric constant and sensor capacitance to their nominal values without altering the sensor properties. In this thesis, dielectric paste annealing was successfully performed over a pure PVDF sensor through high-temperature heat treatment. The increased capacitance induced by gamma radiation effects was significantly decreased after sensor annealing, but sensor re-usability was not confirmed. Low-temperature annealing techniques should be investigated while maintaining the sensor characteristics unchanged. The radiation effects after annealing and re-exposure also need further investigation. Identifying efficient annealing methods that enable repeatable radiation measurements could be the foundation of reusable MEMS sensor fabrication.

Microfabrication of reference capacitors on the same chip for readily subtracting the value of unwanted electrode to handle wafer capacitance in bridge schematics should also be explored.

Finally, more analysis of the dielectric mixture’s penetration depth between interdigitated fingers should be conducted using scanning electron microscopy.

APPENDIX A. ARDUINO SCRIPT

```
#include <Arduino.h>
#include <U8g2lib.h>
#include <EEPROM.h> // memo
#include <Wire.h> // DISPLAY
#include <Adafruit_GFX.h> // DISPLAY
#include <Adafruit_SSD1306.h> // DISPLAY
// DISPLAY

#define SCREEN_WIDTH 128 // OLED display width,  in pixels
#define SCREEN_HEIGHT 64 // OLED display height, in pixels

// declare an SSD1306 display object connected to I2C
Adafruit_SSD1306 oled(SCREEN_WIDTH, SCREEN_HEIGHT, &Wire, -1);

// DISPLAY

int addr = 0; // memo
const int OUT_PIN = A2;
const int IN_PIN = A0;
const float IN_STRAY_CAP_TO_GND = 24.48;
const float IN_CAP_TO_GND  = IN_STRAY_CAP_TO_GND;
const float R_PULLUP = 34.8;
const int MAX_ADC_VALUE = 1023;

void setup() {
  pinMode(OUT_PIN, OUTPUT);
  pinMode(IN_PIN, OUTPUT);
  Serial.begin(9600);
  // DISPLAY
  // initialize OLED display with address 0x3C for 128x64
  if (!oled.begin(SSD1306_SWITCHCAPVCC, 0x3C)) {
    Serial.println(F("SSD1306 allocation failed"));
    while (true);
  }
  delay(2000);         // wait for initializing
  oled.clearDisplay(); // clear display
  // DISPLAY

}

U8G2_SSD1306_128X64_NONAME_F_HW_I2C u8g2(U8G2_R0, /* clock=*/ SCL, /*
data=*/ SDA, /* reset=*/ U8X8_PIN_NONE);  // High speed I2C

// U8G2_SSD1306_128X64_NONAME_F_SW_I2C u8g2(U8G2_R0, /* clock=*/ SCL,
/* data=*/ SDA, /* reset=*/ U8X8_PIN_NONE);    //Low spped I2C

void loop() {

  pinMode(IN_PIN, INPUT);
  digitalWrite(OUT_PIN, HIGH);
  int val = analogRead(IN_PIN);
```

```
  digitalWrite(OUT_PIN, LOW);

  if (val < 1000) {
    pinMode(IN_PIN, OUTPUT);
    float capacitance = (float)val * IN_CAP_TO_GND /
(float)(MAX_ADC_VALUE - val);
    Serial.print(F("Capacitance Value = "));
    Serial.print(capacitance, 3);
    Serial.print(F(" pF ("));
    Serial.print(val);
    Serial.println(F(") "));
    u8g2.clearBuffer();                   // clear the internal memory
    u8g2.setFont(u8g2_font_ncenB08_tr);   // choose a suitable font

    u8g2.drawStr(3, 10, val); // write something to the internal memory
    u8g2.sendBuffer();       // transfer internal memory to the display
    delay(1000);
    oled.clearDisplay(); // clear display
    oled.setTextSize(3);          // text size
    oled.setTextColor(WHITE);     // text color
    oled.setCursor(0, 10);        // position to display
    oled.println(capacitance); // text to display
    oled.display();               // show on OLED
  }

  else {
    pinMode(IN_PIN, OUTPUT);
    delay(1);
    pinMode(OUT_PIN, INPUT_PULLUP);
    unsigned long u1 = micros();
    unsigned long t;
    int digVal;

    do {
      digVal = digitalRead(OUT_PIN);
      unsigned long u2 = micros();
      t = u2 > u1 ? u2 - u1 : u1 - u2;
    } while ((digVal < 1) && (t < 400000L));

    pinMode(OUT_PIN, INPUT);
    val = analogRead(OUT_PIN);
    digitalWrite(IN_PIN, HIGH);
    int dischargeTime = (int)(t / 1000L) * 5;
    delay(dischargeTime);
    pinMode(OUT_PIN, OUTPUT);
    digitalWrite(OUT_PIN, LOW);
    digitalWrite(IN_PIN, LOW);

    float capacitance = -(float)t / R_PULLUP / log(1.0 - (float)val /
(float)MAX_ADC_VALUE);

    Serial.print(F("Capacitance Value = "));
    if (capacitance > 1000.0) {
      Serial.print(capacitance / 1000.0, 2);
      Serial.print(F(" uF"));
```

```
      u8g2.clearBuffer();       // clear the internal memory
      u8g2.setFont(u8g2_font_ncenB08_tr);   // choose a suitable font
      u8g2.drawStr(3, 10, val); // write something to the internal
memory
      u8g2.sendBuffer();                    // transfer internal memory
to the display
      delay(1000);
      oled.clearDisplay(); // clear display
      oled.setTextSize(3);          // text size
      oled.setTextColor(WHITE);     // text color
      oled.setCursor(0, 10);        // position to display
      oled.println(capacitance); // text to display
      oled.display();               // show on OLED
    }
    else {
      Serial.print(capacitance, 2);
      Serial.print(F(" nF"));
      oled.clearDisplay(); // clear display
      oled.setTextSize(3);          // text size
      oled.setTextColor(WHITE);     // text color
      oled.setCursor(0, 10);        // position to display
      oled.println(capacitance); // text to display
      oled.display();               // show on OLED
    }

    Serial.print(F(" ("));
    Serial.print(digVal == 1 ? F("Normal") : F("HighVal"));
    Serial.print(F(", t= "));
    Serial.print(t);
    Serial.print(F(" us, ADC= "));
    Serial.print(val);
    Serial.println(F(")"));
    oled.clearDisplay(); // clear display
    oled.setTextSize(3);          // text size
    oled.setTextColor(WHITE);     // text color
    oled.setCursor(0, 10);        // position to display
    oled.println(capacitance); // text to display
    oled.display();               // show on OLED
    u8g2.clearBuffer();                   // clear the internal memory
    u8g2.setFont(u8g2_font_ncenB08_tr);   // choose a suitable font
    u8g2.drawStr(3, 10, val); // write something to the internal memory
    u8g2.sendBuffer();                    // transfer internal memory
to the display

   }
    delay(1000);
  }
  while (millis() % 1000 != 0);
}
```

THIS PAGE INTENTIONALLY LEFT BLANK

APPENDIX B. MATLAB SCRIPT

```
% Thesis Matlab script for data analysis

clear
clc
close all

read_cptc_msrmts1 =readmatrix('data.csv');
cptc_msrmts1 = read_cptc_msrmts1(:,4);
n1=size(cptc_msrmts1,1);
NumberOfDays1 = n1/(30*60*24) % by using this number calculate the total absorbed dose
abs_dose1 = zeros(n1,1);
for good_msmnts = 1:n1
    abs_dose1(good_msmnts) = good_msmnts*28.46482676/n1; % 28.46 here is the absorbed dose as calculated by using the formulas in Chapter III. It should be adjusted accordingly every time.
end

% % check visually for outliners
plot (abs_dose1,cptc_msrmts1)
set(gca,'FontSize',18)
title('Pure PVDF Raw data - Initial Radiation Exposure')
xlabel('Absorbed dose mGy ')
ylabel('Capacitance [pF]')
legend('Capacitance Values')
```

```
% remove data rows that are outliners
good_msmnts = find(cptc_msrmts1<185 & cptc_msrmts1>130);
good_cptc1 = cptc_msrmts1(good_msmnts);
good_dose1= abs_dose1(good_msmnts);
plot (good_dose1,good_cptc1)
title('Pure PVDF outliner filtering')
xlabel('Absorbed dose mGy ')
ylabel('Capacitance [pF]')
legend('Capacitance Values')

%%%%%%%%%%%%%%%%%%%%%%%%%%%
% fingers only capacitance
idx_col = size(good_cptc1);
base_cpct1= zeros(idx_col(1),1)+80.9641;
good_cptc_fingers_only1 = good_cptc1-base_cpct1;
%%%%%%%%%%%%%%%%%%%%%%%%%%%

Radiation_data = [good_dose1,good_cptc1];
```

```
ploting_dose = movmean(good_dose1,30*60); % 30secs*60min to get mean per
hour
ploting_cpct = movmean(good_cptc1,30*60);
ploting_cpct_fingers_only = movmean(good_cptc_fingers_only1,30*60);
plot(ploting_dose,ploting_cpct)
% points of plot are per hour
title('Pure PVDF Total Capacitance')
xlabel('Absorbed dose mGy ')
ylabel('Capacitance [pF]')
set(gca,'FontSize',18)
%ShadePlot(3.95, 7.9, 'r')

plot(ploting_dose,ploting_cpct_fingers_only)
numBins = 40;
errorplot(ploting_dose, ploting_cpct_fingers_only, numBins)
title('Pure PVDF 60x20 Sensor Finger Capacitance')
xlabel('Absorbed dose mGy ')
ylabel('Capacitance [pF]')
set(gca,'FontSize',18)

min_cpt = min(ploting_cpct);
max_cpt = max(ploting_cpct);
spec = max_cpt-min_cpt;
perc_cpt = (ploting_cpct - min_cpt)*100/spec;
plot(ploting_dose,perc_cpt)
title('Pure PVDF - Initial Exposure (0-100)')
xlabel('Absorbed dose mGy ')
ylabel('Capacitance [pF]')

min_cpt_fingers_only = min(ploting_cpct_fingers_only);
max_cpt_fingers_only = max(ploting_cpct_fingers_only);
spec_fingers_only = max_cpt_fingers_only-min_cpt_fingers_only;
perc_cpt_fingers_only = (ploting_cpct_fingers_only -
67)*100/spec_fingers_only;
plot(ploting_dose,perc_cpt_fingers_only)
title('Pure PVDF - Initial Exposure fingers_only(0-100)')
xlabel('Absorbed dose mGy ')
ylabel('Capacitance [pF]')


ploting_cpct_fingers_only_changes =100*(ploting_cpct_fingers_only-67)./67;
% subtract the unwanted capacity every time

plot(ploting_dose,ploting_cpct_fingers_only_changes)
title('Pure PVDF-60x20 finger capacitance changes')
xlabel('Absorbed dose mGy')
ylabel('Capacitance Change [%]')
set(gca,'FontSize',18)
ShadePlot(3.95, 7.9, 'g')
legend('% capacitance change','working dose area')
```

```
save('ppvdf1st.mat','ploting_dose','perc_cpt')
save('ppvdpercentchange.mat','ploting_dose','ploting_cpct_fingers_only_cha
nges')
```

THIS PAGE INTENTIONALLY LEFT BLANK

LIST OF REFERENCES

[1] E. dos Santos Ferreira and J. S. Souza, "Gamma radiation in ceramic capacitors: a study for space missions," *J. Phys. Conf. Ser.*, vol. 911, Oct. 2017, doi: 10.1088/1742-6596/911/1/012004.

[2] E. J. Polidan *et al.*, "A study of hot pixel annealing in the Hubble Space Telescope Wide Field Camera 3 CCDs," *NASA/NEPP*, Accessed: Nov. 06, 2022. Available: https://nepp.nasa.gov/DocUploads/F342903F-8809-4B1E-83E4F3F4CAC2889A/Polidan_hotpix.pdf

[3] White, I. I. *et al.*, "An overview of basic radiation effects on polymers and glasses," *U.S. D.O.E.*, Washington, DC, USA, 1 Sept. 2013. Available: https://www.osti.gov/servlets/purl/1671997

[4] L. Zeininger, M. He, S. T. Hobson, and T. M. Swager, "Resistive and capacitive γ-ray dosimeters based on triggered depolymerization in carbon nanotube composites," *ACS Sens*., vol. 3, no. 5, May 2018, doi: 10.1021/acssensors.8b00108.

[5] J. Shi *et al.*, "Radiation-induced charge trapping in Si-MOS capacitors with HfO2/SiO2 gate dielectrics," *Nucl. Instrum. Methods Phys. Res. Sect. B Beam Interact. Mater. At*., vol. 479, Sep. 2020, doi: 10.1016/j.nimb.2020.06.039.

[6] S. Malekie and F. Ziaie, "Study on a novel dosimeter based on polyethylene–carbon nanotube composite," *Nucl. Instrum. Methods Phys. Res. Sect. Accel. Spectrometers Detect. Assoc. Equip.*, vol. 791, Aug. 2015, doi: 10.1016/j.nima.2015.04.031.

[7] M. T. Alabsy *et al*., "Gamma-Ray Attenuation and Exposure Buildup Factor of Novel Polymers in Shielding Using Geant4 Simulation," *Materials*, vol. 14, no. 17, Sep. 2021, doi: 10.3390/ma14175051.

[8] A. Kaymaz *et al.*, "Investigation of gamma-irradiation effects on electrical characteristics of Al/(ZnO–PVA)/p-Si Schottky diodes using capacitance and conductance measurements," *J. Mater. Sci. Mater. Electron.,* vol. 31, no. 11, Jun. 2020, doi: 10.1007/s10854-020-03370-2.

[9] O. Korostynska *et al*., "Radiation-induced changes in the electrical properties of carbon filled PVDF thick films," *Mater. Sci. Eng. B*, vol. 141, no. 3, Aug. 2007, doi: 10.1016/j.mseb.2007.06.025.

[10] H. M. Said, "Effects of gamma irradiation on the crystallization, thermal and mechanical properties of poly(l-lactic acid)/ethylene-co-vinyl acetate blends*," J. Radiat. Res. Appl. Sci.*, vol. 6, no. 2, Oct. 2013, doi: 10.1016/j.jrras.2013.10.001.

[11] K. Arshak and O. Korostynska, "Preliminary studies of properties of oxide thin/ thick films for gamma radiation dosimetry," *Mater. Sci. Eng. B*, vol. 107, no. 2, Mar. 2004, doi: 10.1016/j.mseb.2003.11.014.

[12] K. Arshak *et al.*, "Thin and thick films of metal oxides and metal phthalocyanines as gamma radiation dosimeters," *IEEE Trans. Nucl. Sci*., vol. 51, no. 5, Oct. 2004, doi: 10.1109/TNS.2004.834718.

[13] G. Ribeiro *et al.*, "Gamma irradiation effects on poly(vinylidene fluoride) films," *in 2009 Int. Nucl. Atl. Conf. (INAC),* Rio de Janeiro, Brazil, Sept. 27, 2009.

[14] L. Zeininger *et al.*, "Resistive and capacitive g-ray dosimeters based on triggered depolymerization in carbon nanotube composites," *ACS Sensors*, vol. 3, no. 5, 2018. Available: https://doi.org/10.1021/acssensors.8b00108

[15] R. A. Kimble *et al.*, "Radiation damage effects on the CCD detector of the space telescope imaging spectrograph," *UV Opt. IR Space Telesc. Instrum.,* 2000.

[16] Mirion, "EDIS-1™ Environmental Direct Ion Storage dosimeter," Accessed: Sep. 30, 2023. Available: https://www.mirion.com/products/technologies/health-physics-radiation-safety-instruments/dosimetry-telemetry-systems/passive-dosimetry-systems/edis-1-environmental-direct-ion-storage-dosimeter

[17] Mega Depot, "Buy radiation meters." Accessed: Sep. 30, 2023. Available: https://megadepot.com/catalog/test-equipment/radiation-meters

[18] Fisher Scientific, "Radiation detectors," Accessed: Sep. 30, 2023. Available: https://www.fishersci.com/us/en/browse/90150462/Radiation-Detectors

[19] F. Alves, R. Rabelo, and G. Karunasiri, "Dual band MEMS directional acoustic sensor for near resonance operation," *Sensors*, vol. 22, no. 15, Jul. 2022, doi: 10.3390/s22155635.

[20] F. Laemer and A. Urban, "Challenges, developments and applications of silicon deep reactive ion etching," *Microelectron. Eng.,* vol. 67, 2003.

[21] Nordion, "GT gamma compatible materials." Accessed: Sep. 30, 2023. Available: https://www.nordion.com/wp-content/uploads/2014/10/GT_Gamma_Compatible_Materials.pdf

[22] R. Ram *et al.*, "Electrical properties of polyvinylidene fluoride (PVDF)/multi-walled carbon nanotube (MWCNT) semi-transparent composites: Modelling of DC conductivity," *Compos. Part Appl. Sci. Manuf.,* vol. 69, Feb. 2015, doi: 10.1016/j.compositesa.2014.11.003.

[23] B. P. McHale, "Low cost, disposable MEMS radiation detectors using gamma sensitive polymers," M.S. thesis, NPS, Monterey, CA, USA, Jun. 2020.

[24] "Caesium-137 Atom, Includes 55 Protons 55 Electrons 82 Neutrons." *Wikimedia Commons,* 13 Nov. 2021, Accessed: Oct. 25, 2023. Available: https://commons.wikimedia.org/wiki/File:Caesium-137.svg

[25] Eckert & Ziegler, "Point and tube sources (gamma and electron emitters)," Accessed: Nov. 06, 2022. Available: https://www.gammadata.se/assets/Uploads/03-point-and-tube-source.pdf

[26] J. Viegas, L. A. Silva, A. M. S. Batista, C. A. Furtado, J. P. Nascimento, and L. O. Faria, "Increased X-ray attenuation efficiency of graphene-based nanocomposite," *Ind. Eng. Chem. Res*., vol. 56, no. 41, Oct. 2017, doi: 10.1021/acs.iecr.7b02711.

[27] J. Robertson, "High dielectric constant oxides," *Eur. Phys. J. Appl. Phys.,* vol. 28, no. 3, Dec. 2004, doi: 10.1051/epjap:2004206.

[28] A. N. Arshad, M. H. M. Wahid, M. Rusop, W. H. A. Majid, R. H. Y. Subban, and M. D. Rozana, "Dielectric and structural properties of poly(vinylidene fluoride) (PVDF) and poly(vinylidene fluoride-trifluoroethylene) (PVDF-TrFE) filled with Magnesium Oxide Nanofillers," *J. Nanomater.,* vol. 2019, Apr. 2019, doi: 10.1155/2019/5961563.

[29] S. O. Kasap, *Principles of electronic materials and devices,* 4th ed. New York, NY, USA: McGraw-Hill Inc, 2018.

[30] V. Tiwari and G. Srivastava, "Effect of thermal processing conditions on the structure and dielectric properties of PVDF films," *J. Polym. Res.,* vol. 21, no. 11, Nov. 2014, doi: 10.1007/s10965-014-0587-0.

[31] "A plot of normally-distributed white noise." *Wikimedia Commons*, 21 Apr. 2008. Accessed: Oct. 25, 2023. Available: https://commons.wikimedia.org/wiki/File:White-noise.png

THIS PAGE INTENTIONALLY LEFT BLANK

INITIAL DISTRIBUTION LIST

1. Defense Technical Information Center
   Ft. Belvoir, Virginia

2. Dudley Knox Library
   Naval Postgraduate School
   Monterey, California

DUDLEY KNOX LIBRARY

NAVAL POSTGRADUATE SCHOOL

WWW.NPS.EDU

WHERE SCIENCE MEETS THE ART OF WARFARE